Check for updates

Numerical optimization of Rb$_2$AuScBr$_6$ and Rb$_2$AuScCl$_6$-based lead-free perovskite solar cells: device engineering and performance mapping

Md. Al-Amin,[a] A. Haque,[a] S. Mahmud, [iD] *[a] M. M. Hossain, [iD] [b] M. M. Uddin[b] and M. A. Ali [iD] *[b]

Perovskite solar cells (PSCs) exhibit significant potential for next-generation photovoltaic technology, integrating high power conversion efficiency (PCE), cost-effectiveness, and tunable optoelectronic properties. This report presents a comprehensive numerical optimization of Rb$_2$AuScBr$_6$ and Rb$_2$AuScCl$_6$-based PSCs, with particular emphasis on the influence of electron transport layers (ETLs) and critical device parameters. The configuration ITO/TiO$_2$/Rb$_2$AuScBr$_6$/CBTS/Ni achieves a PCE of 27.49%, whereas the configuration ITO/WS$_2$/Rb$_2$AuScCl$_6$/CBTS/Ni attains 22.41%, thereby underscoring the high efficiency of these lead-free materials. Device performance is markedly improved through increased perovskite layer thickness and reduced defect density. Further stabilization of performance is achieved by optimizing electron affinity, series resistance, and shunt resistance. Additionally, thermal stability is enhanced through the adjustment of operational temperature. The superior PCE observed in Rb$_2$AuScBr$_6$ is ascribed to the selection of the ETL, an optimal band gap, absorber layer thickness, lower defect density, and appropriate contact interfaces. Overall, these Rb$_2$AuScBr$_6$ and Rb$_2$AuScCl$_6$ perovskites demonstrate exceptional promise for practical, efficient, and stable PSC applications, thereby encouraging further experimental validation and device engineering.

1. Introduction

The growing global need for energy, fueled by rapid population growth and industrial development, has spurred a concerted search for sustainable and eco-friendly energy sources.[1] Among these, solar energy provides an ample, renewable resource that can be harnessed to overcome the constraints of fossil fuels in a cost-efficient manner.[2] With its unique characteristics and advantages, photovoltaic (PV) technology is a rather efficient method for converting sunlight into electricity, which presents low operation cost and less environmental pollution than other traditional energy generation methods.[3]

Perovskite materials have garnered widespread attention in recent years owing to their outstanding light-harvesting capabilities, tunable band gaps, and exceptional power conversion efficiencies (PCEs).[4] Within this family, double perovskites—typically denoted A$_2$BB′X$_6$ (X = halide)—offer a particularly promising avenue.[5] Unlike traditional single-cation ABX$_3$ perovskites, their expanded B-site cation combinations facilitate precise tuning of

electronic structures and band gaps. This flexibility enables the creation of lead-free, environmentally benign alternatives with band gaps better matched to the solar spectrum.[6,7]

One notable candidate, Cs$_2$AgBiBr$_6$, exhibits a large but stable indirect band gap of around 2.2 eV. Treating conventional perovskites with Cs$_2$AgBiBr$_6$ nanoparticles has yielded enhanced stability and an impressive PCE of 19.52%, underscoring the advantage of its passivation capabilities.[8] Through compositional engineering, this band gap can be further tuned: Tl-doping narrows it to 1.57 eV, while Sb-for-Bi substitution reaches 1.86 eV, improving absorption and photovoltaic potential.[9]

Similarly, Cs$_2$AgInBr$_6$ has been explored using first-principles and optical studies, revealing a direct band gap of approximately 1.427 eV and excellent absorption ($>10^4$ cm^{-1}), positioning it as a viable PV absorber.[10] Another intriguing family, A$_2$AgIrCl$_6$ (A = Cs, Rb, K), displays direct band gaps of about 1.43–1.55 eV (Cs$_2$ = 1.43 eV; Rb$_2$ = 1.50 eV; K_2 = 1.55 eV), alongside low effective electron masses and strong visible-light absorption, making them highly promising for solar cell applications.[11]

A different strategy involves alloying: in Cs$_2$Ag(Sb$_x$Bi$_{1-x}$)Br$_6$, band gaps reduce below those of the pure end members down to about 2.08 eV when $x = 0.9$, thanks to band-gap bowing from Sb–Bi orbital mixing.[12] Additional studies have explored Cs$_2$AgBiBr$_6$ doped with aluminum: the pristine material shows E_g

[a] Department of Electrical and Electronic Engineering, Jatiya Kabi Kazi Nazrul Islam University (JKKNIU), Mymensingh-2224, Bangladesh. E-mail: shuaib.eee.iu@gmail.com

[b] Advanced Computational Materials Research Laboratory, Department of Physics, Chittagong University of Engineering and Technology (CUET), Chattogram-4349, Bangladesh

$\approx$ 1.91 eV, whereas Al-doped films exhibit a slightly lowered E_g of 1.82 eV, resulting in improved device metrics (PCE from ~3.02% to ~3.40%).[13] Another notable double perovskite, $Cs_2CuBiCl_6$, has emerged *via* SCAPS-1D simulation as a lead-free absorber with high predicted efficiencies; optimized devices yielded PCE up to 24.51%, V_{oc} = 1.73 V, and J_{sc} = 32.82 mA cm^{-2}.[14] These theoretical models affirm the material's considerable promise for durable, high-performance photovoltaics.

Collectively, these studies underscore the diverse strategies available—doping, substitution, alloying, and novel compounds—to engineer double perovskites with direct, suitably low band gaps (spanning ~1.4 to 2.2 eV). Realizing these tunable properties positions them as key materials for next-generation, lead-free, high-efficiency solar technologies, potentially even surpassing conventional limits.[15] Several electron transport layers (ETLs) have been explored to improve the performance of perovskite solar cells (PSCs). WS_2, a transition metal dichalcogenide, offers suitable conduction band alignment and decent electron mobility, enhancing power conversion efficiency (PCE).[16] ZnO, with its wide band gap (~3.3 eV), high electron mobility, and transparency, is attractive, though interfacial reactions with perovskites may cause stability issues requiring surface modification.[17] PCBM, a fullerene derivative, is widely used for its strong electron-accepting ability and reduced recombination losses.[18] TiO_2 is the most common ETL due to its band alignment, chemical stability, and transparency, but its low electron mobility and recombination tendencies necessitate surface treatments or doping.[19] IGZO, with high electron mobility and optical transparency, and C_{60}, with strong electron transport properties, are also promising ETLs.[20,21]

For hole transport layers (HTLs), CBTS has demonstrated strong potential owing to its favorable energy level alignment and ability to enhance hole extraction and stability.[22] Other candidates include CdTe, CuI, PTAA, P3HT, and PEDOT : PSS, each offering distinct advantages such as high hole mobility, thermal stability, or compatibility with perovskite layers, though limitations like poor conductivity or stability often require doping or modification.[23–27]
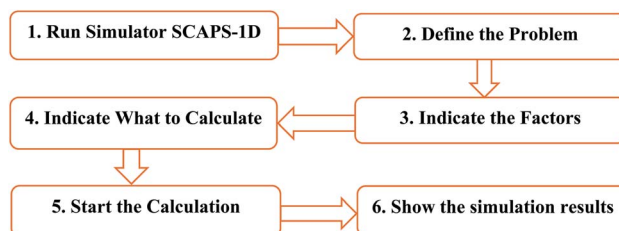
In this work, we present the simulation and optimization of lead-free double perovskite solar cells based on $Rb_2AuScBr_6$ and $Rb_2AuScCl_2$ absorbers. Using SCAPS-1D, we systematically investigate n–i–p planar heterojunction structures with various ETLs (IGZO, WS_2, ZnO, PCBM, C_{60}, and TiO_2) and HTLs (CBTS, CdTe, CuI, PTAA, P_3HT, and PEDOT : PSS). Among the HTLs, CBTS demonstrates superior performance for both absorbers. Device parameters such as absorber thickness, defect density, resistances, and operating temperature are tuned to optimize photovoltaic performance. The results indicate that these double perovskite materials hold great promise for high-efficiency, environmentally friendly PSCs, contributing to the development of next-generation renewable energy technologies.[28–31]

2. Methodology

The numerical studies of this work were performed using the Solar Cell Capacitance Simulator (SCAPS-1D), the widely used one-dimensional solar cell simulation tool developed at the University

of Ghent, Belgium. Data analysis of a wide range of photovoltaic device parameters, such as energy band alignment, charge transport mechanisms, recombination losses, and current–voltage (*J*–*V*) characteristics, can be performed through SCAPS-1D.[32]

The simulation process adheres to the usual operating routine of SCAPS-1D as follows:[33].

The SCAPS-1D simulator is built upon three key semiconductor equations: Poisson's equation, the electron continuity equation, and the hole continuity equation. These equations define how electric potential and charge carriers (electrons and holes) behave and distribute within a semiconductor device. SCAPS-1D numerically solves these equations to model the internal physics of solar cells and predict their performance. Poisson's equation is given as:[34–36]

$$\frac{\partial}{\partial x}\left(\varepsilon(x)\frac{\partial \psi}{\partial x}\right) = \frac{-q}{\varepsilon_o}\left[p - n + N_D^+ - N_A^- + \frac{\rho_{def}(n,p)}{q}\right] \quad (1)$$

Here, ψ (psi) is the electric potential, ε (epsilon) is the material's ability to store electric charge (called the dielectric constant), q is the charge of an electron, and ρ (def) is the charge from defects inside the material.

Eqn (2) and (3) are used to show how free electrons and free holes are conserved or balanced inside the solar cell device.

$$\frac{\partial p}{\partial t} = \frac{1}{q}\frac{\partial J_p}{\partial x} + (G_p - R_p) \quad (2)$$

$$\frac{\partial n}{\partial t} = \frac{1}{q}\frac{\partial J_n}{\partial x} + (G_n - R_n) \quad (3)$$

Here, $\frac{\partial p}{\partial t}$ is the rate of change of hole concentration p with time, q is the charge of an electron or hole, $\frac{\partial J_p}{\partial x}$ is the change of hole current density J_p over distance x, G_p is the hole generation rate, R_p is the hole recombination rate, $\frac{\partial n}{\partial t}$ is the rate of change of electron concentration, $\frac{\partial J_n}{\partial x}$ is the change of electron current density J_n over distance x, G_n is the electron generation rate and R_n is the electron recombination rate.

Eqn (4) and (5) are used to calculate the drift current and the diffusion current.

$$J_n = q\mu_n n\varepsilon + qD_n\delta n \quad (4)$$

$$J_P = q\mu_p n\varepsilon - qD_p\delta p \quad (5)$$

where μ_n is the mobility of electrons, μ_p is the mobility of holes and the diffusion coefficient (D_n for electrons, D_p for holes) shows how fast they spread out from high to low concentration.

3. Results & discussion

The design configuration of the $Rb_2AuScBr_6$-and $Rb_2AuScCl_6$-based perovskite solar cell (PSC) follows an n–i–p planar heterojunction structure (Fig. 1), where the ETL is in the n-region, the perovskite absorber layer in the i-region, and the HTL in the p-region. When exposed to sunlight, excitons (electron–hole pairs) are generated within the perovskite layer.[37,38] The built-in electric field at the interfaces aids in exciton dissociation, directing electrons toward the n-layer and holes toward the p-layer for efficient charge extraction.[39] Indium-doped tin oxide (ITO) is used as the transparent conductive front contact. Different ETL materials, including IGZO, WS_2, ZnO, PCBM, C_{60}, and TiO_2, are investigated to optimize electron transport. The $Rb_2AuScCl_6$ and $Rb_2AuScBr_6$ perovskites serve as the absorber layer, enabling efficient light absorption. Among 36 different ETL–HTL combinations, CBTS is selected as the HTL due to its superior hole transport properties and compatibility with the absorber. The Ni completes the device structure and collects the extracted charges.

Simulations were performed under AM1.5 G solar spectrum conditions to analyze the impact of different ETL and HTL combinations, aiming to determine the most efficient structure. The study explores lead-free, stable perovskite materials as potential candidates for environmentally friendly and high-performance solar cells.
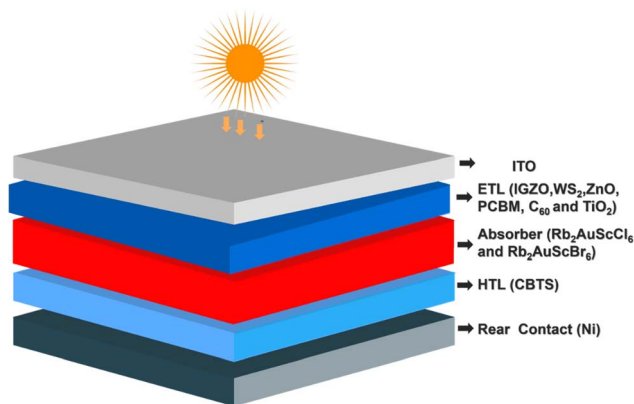

Fig. 1 The design configuration of the $Rb_2AuScCl_6$ and $Rb_2AuScBr_6$-based PSC.

To determine the input parameters required for the equations mentioned above, the following calculation procedures are employed, with all relevant values detailed in Tables 1–3. Eqn (6) defines the carrier's effective mass m^* in terms of the curvature of the energy–momentum relation:[40]

$$m^* = \frac{\hbar^2}{(\mathrm{d}^2E/\mathrm{d}K^2)} \tag{6}$$

where $\hbar$ is the reduced Planck constant (1.05×10^{-34} J s^{-1}) and $\mathrm{d}^2E/\mathrm{d}K^2$ is the second derivative of the band energy E with respect to the wavevector k.

Eqn (7) and (8) then use these effective masses to compute the effective density of states in the valence band (N_v) and conduction band (N_c), respectively, at temperature T:

$$N_v = 2\frac{(2\pi\, m_h^* K_B T)^{3/2}}{h^3} \approx 2.5409 \times 10^{19} \left(\frac{m_h^*}{m_0}\right)^{3/2} \tag{7}$$

$$N_c = 2\frac{(2\pi m_e^* K_B T)^{3/2}}{h^3} \approx 2.5409 \times 10^{19} \left(\frac{m_e^*}{m_0}\right)^{3/2} \tag{8}$$

where K_B is Boltzmann's constant, h is Planck's constant, and m_h^* and m_e^* are the hole and electron effective masses. Eqn (9) and (10) relate the carrier mobilities μ_e (electron mobility) and μ_h (hole mobility) to the carrier charge q, the relaxation time τ, and the respective effective masses:[41]

$$\mu_e = \frac{q\tau}{m_e} \tag{9}$$

$$\mu_h = \frac{q\tau}{m_h} \tag{10}$$

3.1. Absorber material parameters and band alignment of $Rb_2AuScBr_6$ and $Rb_2AuScCl_6$-based absorbers with different ETLs and HTL

The electronic and optical suitability of $Rb_2AuScBr_6$ and $Rb_2AuScCl_6$ as absorber materials has been theoretically validated through density functional theory (DFT) calculations. DFT results confirm indirect band gaps of 1.71 eV and 1.93 eV,[45] respectively, within the optimal photovoltaic range (1.4–2.2 eV), with high absorption coefficients ($\approx 10^6$ cm^{-1}) and low reflectivity (<15%), indicating their potential as efficient light-absorbing semiconductors.

Table 1 Input parameters of HTLs[42]

Parameters	CBTS	CdTe	P3HT	PEDOT : PSS	PTAA	CuI
t (nm)	100	200	50	50	150	100
E_g (eV)	1.9	1.5	1.7	1.6	2.96	3.1
X (eV)	3.6	3.9	3.5	3.4	2.3	2.1
E_r	5.4	9.4	3	3	9	6.5
N_C (cm^{-3})	2.2×10^{18}	8×10^{17}	2.0×10^{21}	2.2×10^{18}	2.0×10^{21}	2.8×10^{19}
N_V (cm^{-3})	1.8×10^{19}	1.8×10^{19}	2.0×10^{21}	1.8×10^{19}	2.0×10^{21}	1×10^{19}
μ_e (cm^2 V^{-1} s^{-1})	30	3.2×10^2	1.8×10^{-3}	4.5×10^{-2}	1	100
μ_h (cm^2 V^{-1} s^{-1})	10	4×10^1	1.86×10^{-2}	4.5×10^{-2}	40	43.9
N_D (cm^{-3})	0	0	0	0	0	0
N_A (cm^{-3})	10^{18}	2.0×10^{14}	10^{18}	10^{18}	10^{18}	10^{18}
N_t (cm^{-3})	10^{15}	10^{15}	10^{15}	10^{15}	10^{15}	10^{15}

Table 2 Input parameters of ETLs[43]

Parameters	Ws$_2$	ZnO	TiO$_2$	PCBM	IGZO	C$_{60}$
t (nm)	100	50	30	50	30	50
E_g (eV)	1.8	3.3	3.2	2	3.05	1.7
X (eV)	3.95	4	4	3.9	4.16	3.9
E_r	13.6	9.00	9	3.9	10	4.2
N_C (cm^{-3})	1×10^{18}	3.7×10^{18}	2.0×10^{18}	2.5×10^{21}	5×10^{18}	8×10^{19}
N_V (cm^{-3})	2.4×10^{19}	1.8×10^{19}	1.8×10^{19}	2.5×10^{21}	5×10^{18}	8×10^{19}
μ_e (cm^2 V^{-1} s^{-1})	100	100	20	0.2	15	8×10^{-2}
μ_h (cm^2 V^{-1} s^{-1})	100	250	10	0.2	0.1	3.5×10^{-3}
N_D (cm^{-3})	10^{18}	10^{18}	9×10^{16}	2.93×10^{17}	10^{17}	10^{17}
N_A (cm^{-3})	0	0	0	0	0	0
N_t (cm^{-3})	10^{15}	10^{15}	10^{15}	10^{15}	10^{15}	10^{15}

Table 3 Input parameters of Front contact (ITO) and Absorber Rb$_2$-AuScCl$_6$ and Rb$_2$AuScBr$_6$ for initial optimization[44] ^{a}

Parameters	ITO	Rb$_2$AuScBr$_6$	Rb$_2$AuScCl$_6$
t (nm)	500	1200	1200
E_g (eV)	3.5	1.71	1.93
X (eV)	4	3.95	3.75
E_r	9	6.34	6.01
N_C (cm^{-3})	2.2×10^{18}	1.33×10^{18}	1.94×10^{18}
N_V (cm^{-3})	1.8×10^{19}	4.56×10^{18}	4.59×10^{18}
μ_e (cm^2 V^{-1} s^{-1})	20	83.20	64.71
μ_h (cm^2 V^{-1} s^{-1})	10	43.14	36.40
N_D (cm^{-3})	10^{21}	0	0
N_A (cm^{-3})	0	10^{15}	10^{15}
N_t (cm^{-3})	10^{15}	10^{15}	10^{15}

^{a} [t = thickness, X = electron affinity, E_r = dielectric relative permittivity, N_c and N_v = effective density of states in the conduction band and valence band, μ_e and μ_h = electron mobility and hole mobility, and N_D, N_A, and N_t = donor, acceptor, and defect density in Tables (1–3)].

Fig. 2(a) illustrates the band alignment of the Rb$_2$AuScBr$_6$ absorber with various ETLs and HTLs. The energy band offsets at these interfaces are critical for efficient charge carrier separation and transport, directly influencing solar cell performance. To explore the dynamics of charge carriers, the conduction band minimum (CB), valence band maximum (VB), and quasi-Fermi levels for electrons (F_n) and holes (F_p) are analyzed. Rb$_2$AuScBr$_6$ has a conduction band at 1.47574 eV, a valence band at −0.23426 eV, and a bandgap (E_g) of 1.71 eV, which favors photon absorption and contributes to better overall power conversion efficiency (PCE). Among the ETLs, TiO$_2$ and ZnO exhibit closely matched conduction band levels (−3.11 eV and −3.26 eV), allowing comparable electron injection capabilities.

WS$_2$ (−1.78 eV) and PCBM (−1.74 eV) also demonstrate suitable alignments, making them promising ETL alternatives. IGZO (−2.94 eV) and C$_{60}$ (−1.49 eV) offer diverse work functions and conduction band offsets, introducing flexibility for device tuning.

On the HTL side, CBTS (conduction band edge ~0.15 eV) aligns effectively with the absorber, promoting smooth hole extraction. Other HTLs such as P3HT (0.45 eV), CdTe (0.25 eV), CuI (0.45 eV), PEDOT : PSS (0.65 eV), and PTAA (0.39 eV) exhibit various energy level alignments, influencing hole extraction efficiency. CuI and PTAA, in particular, have high valence band energies (3.55 eV and 3.35 eV, respectively), favoring hole mobility. Nickel (Ni), with a work function of 5.5 eV, ensures efficient hole collection by aligning well with these HTLs, reducing recombination at the back contact.

Fig. 2(b) shows the band alignment of the Rb$_2$AuScCl$_6$ absorber with the same ETLs and HTLs. While the alignment is generally analogous to the Rb$_2$AuScBr$_6$ system, subtle differences are observed in the energy levels, which slightly alter charge transport. Rb$_2$AuScCl$_6$ has a conduction band at 1.67588 eV, a valence band at −0.25412 eV, and a larger bandgap of 1.93 eV. Due to the wider bandgap, Rb$_2$AuScCl$_6$ tends to absorb fewer photons in the solar spectrum, which can reduce current generation and thus lower the overall PCE compared to its Br-based counterpart.[46–48]

3.2. Optimization of the HTL layer and the ETL layer

The selection of optimal ETL and HTL materials for the Rb$_2$-AuScBr$_6$-and Rb$_2$AuScCl$_6$-based perovskite solar cells was guided by both photovoltaic performance parameters (PCE, V_{oc}, J_{sc}, and FF) and key physical considerations, including energy-band alignment, carrier mobility, defect density, material stability, and interfacial charge-transport behavior. Efficient charge extraction requires precise band matching, wherein the conduction band of the ETL lies slightly below that of the absorber to facilitate electron transfer while suppressing hole leakage, and the valence band of the HTL aligns closely with that of the absorber to enable rapid hole transport. Such optimized alignment minimizes interfacial barriers and recombination losses, thereby enhancing V_{oc}, J_{sc}, and FF. Secondary selection criteria included high carrier mobility, low trap density, and strong chemical and thermal stability to ensure robust and loss-free charge transport pathways. Among the investigated materials, IGZO and WS$_2$ emerged as the most effective ETLs due to their high electron mobility, low defect density, and superior environmental stability, while CBTS proved to be an excellent HTL owing to its favorable energy-level alignment, high hole mobility, and long-term durability. Furthermore, optimized acceptor doping in the absorber enhanced the internal electric field, promoting efficient charge separation and reducing recombination. The IGZO/CBTS
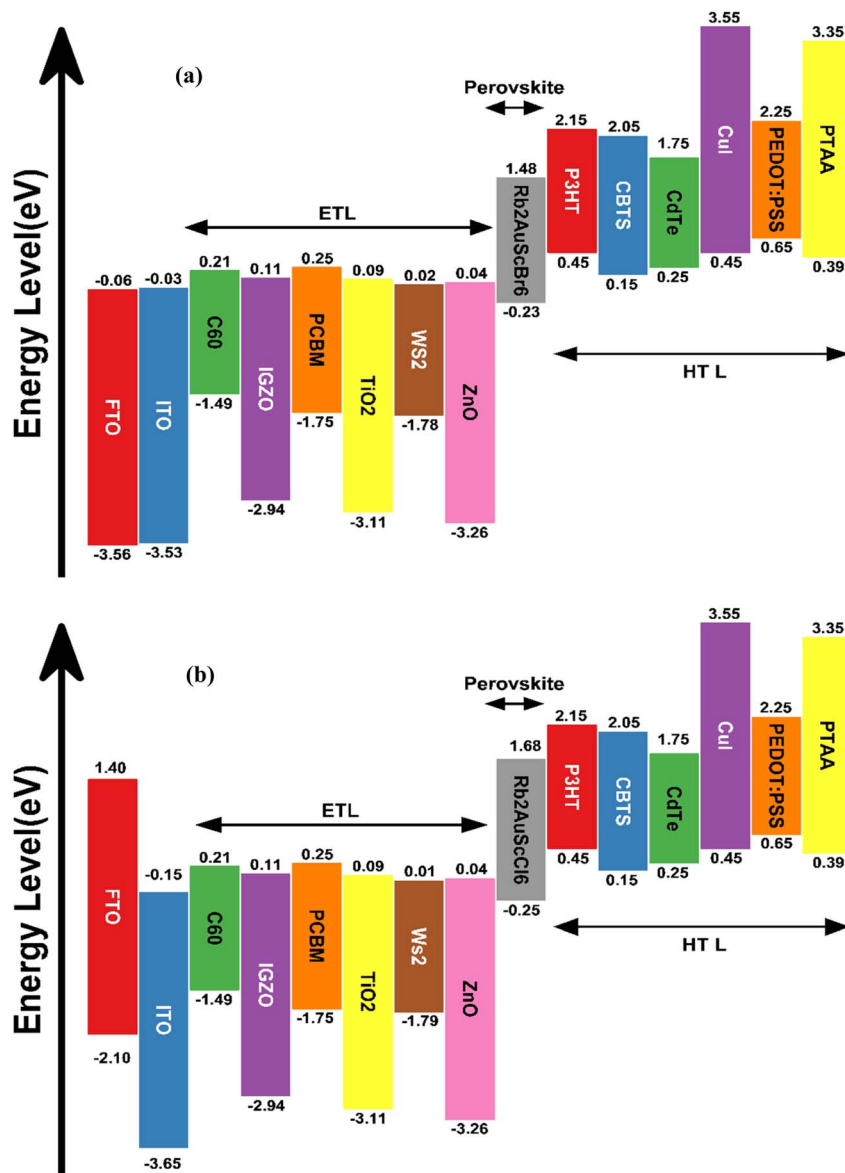
Fig. 2 Energy band alignment between the different ETL and HTL materials of (a) $Rb_2AuScBr_6$ absorber and (b) $Rb_2AuScCl_6$ absorber.

combination for the $Rb_2AuScBr_6$ device and the WS_2/CBTS combination for the $Rb_2AuScCl_6$ device provided the most favorable band alignment and carrier extraction pathways, leading to the highest PCEs.

The variations in efficiency among different ETL/HTL configurations can be primarily attributed to differences in interfacial recombination, which were modeled through interface defect densities ($N_t = 10^{15}$ cm^{-3}). These optimized configurations exhibited lower recombination losses owing to improved interfacial quality and energetically well-matched interfaces.

3.2.1. Selection of ETL and HTL for $Rb_2AuScBr_6$-based solar cells. Fig. 3(a) shows that using WS_2 as ETL and CBTS as HTL results in a PCE of 23.68%, with an open-circuit voltage (V_{oc}) of 1.258 V, short-circuit current density (J_{sc}) of 21.433 mA cm^{-2}, and fill factor (FF) of 87.85%. WS_2, a two-dimensional

transition metal dichalcogenide, exhibits high electron mobility and favorable energy level alignment with the perovskite absorber, enabling efficient electron extraction. This combination maintains stable charge transport and hinders recombination, leading to high efficiency. However, the lower V_{oc} and FF than that of IGZO translate to slightly lower PCE. Fig. 3(b) depicts that using ZnO as the ETL and CBTS as the HTL lead to PCE 23.65% ($V_{oc} = 1.257$ V, $J_{sc} = 21.414$ mA cm^{-2}, FF = 87.83%). ZnO is a common ETL with high electron transport properties, but its electron mobility being lower than IGZO and WS_2, makes its efficiency take a hit. Even though ZnO has good performance, its interface properties and energy level alignment are not as good as IGZO, resulting in a relatively low PCE. In Fig. 3(c) achieves 23.57% PCE is achieved with $V_{oc} = 1.256$ V, $J_{sc} = 21.378$ mA cm^{-2}, and FF = 87.80% with a combination of PCBM ETL and CBTS HTL. A well-known electron acceptor,

(a) WS2

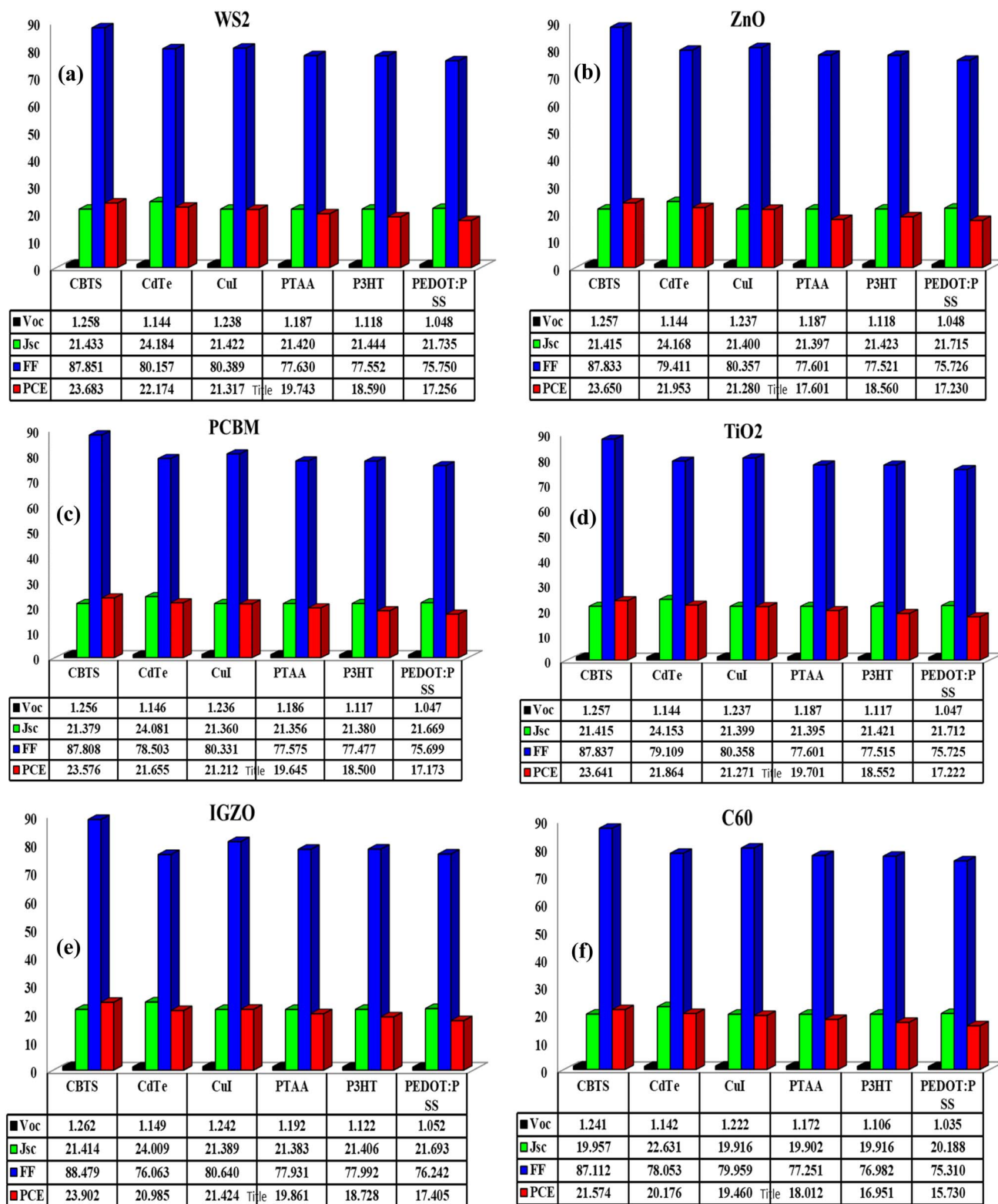|	CBTS	CdTe	CuI	PTAA	P3HT	PEDOT:PSS
Voc	1.258	1.144	1.238	1.187	1.118	1.048
Jsc	21.433	24.184	21.422	21.420	21.444	21.735
FF	87.851	80.157	80.389	77.630	77.552	75.750
PCE	23.683	22.174	21.317	19.743	18.590	17.256

(b) ZnO

	CBTS	CdTe	CuI	PTAA	P3HT	PEDOT:PSS
Voc	1.257	1.144	1.237	1.187	1.118	1.048
Jsc	21.415	24.168	21.400	21.397	21.423	21.715
FF	87.833	79.411	80.357	77.601	77.521	75.726
PCE	23.650	21.953	21.280	17.601	18.560	17.230

(c) PCBM

	CBTS	CdTe	CuI	PTAA	P3HT	PEDOT:PSS
Voc	1.256	1.146	1.236	1.186	1.117	1.047
Jsc	21.379	24.081	21.360	21.356	21.380	21.669
FF	87.808	78.503	80.331	77.575	77.477	75.699
PCE	23.576	21.655	21.212	19.645	18.500	17.173

(d) TiO2

	CBTS	CdTe	CuI	PTAA	P3HT	PEDOT:PSS
Voc	1.257	1.144	1.237	1.187	1.117	1.047
Jsc	21.415	24.153	21.399	21.395	21.421	21.712
FF	87.837	79.109	80.358	77.601	77.515	75.725
PCE	23.641	21.864	21.271	19.701	18.552	17.222

(e) IGZO

	CBTS	CdTe	CuI	PTAA	P3HT	PEDOT:PSS
Voc	1.262	1.149	1.242	1.192	1.122	1.052
Jsc	21.414	24.009	21.389	21.383	21.406	21.693
FF	88.479	76.063	80.640	77.931	77.992	76.242
PCE	23.902	20.985	21.424	19.861	18.728	17.405

(f) C60

	CBTS	CdTe	CuI	PTAA	P3HT	PEDOT:PSS
Voc	1.241	1.142	1.222	1.172	1.106	1.035
Jsc	19.957	22.631	19.916	19.902	19.916	20.188
FF	87.112	78.053	79.959	77.251	76.982	75.310
PCE	21.574	20.176	19.460	18.012	16.951	15.730

Fig. 3 HTL & ETL selection for $Rb_2AuScBr_6$ of (a) WS_2 (b) ZnO (c) PCBM, (d) TiO_2, (e) IGZO and (f) C_{60} with HTL of CBTS, CdTe, CuI, PTAA, P3HT and PEDOT : PSS.

PCBM, has much lower electron mobility than IGZO, WS_2, and ZnO, resulting in lower efficiency. Although the fill factor is indeed high, the reduced electron mobility results in a mild drop of the charge collection efficiency, which ends up decreasing the PCE. Fig. 3(d) demonstrates TiO_2 as ETL and CBTS as HTL yields a PCE of 23.64% ($V_{oc} = 1.257$ V, $J_{sc} = 21.415$

mA cm^{-2}, and FF = 87.83%). TiO$_2$ is known to have great electron transport properties and high stability, which makes it a widespread choice for ETL. Nevertheless, due to its low conductivity and moderate energy level alignment, its efficiency is slightly lower than that obtained with WS$_2$ and IGZO. TiO$_2$ is not considered the most optimal in terms of charge transport properties, even though it is widely used. Fig. 3(e) shows that the best performance of 23.90% PCE achieved with IGZO ETL and CBTS HTL, V_{oc} = 1.262 V, J_{sc} = 21.414 mA cm^{-2}, and FF = 88.48%. IGZO possesses good electron transport properties, thanks to its high electron mobility, which allows for rapid extraction of charge. Also, its low trap density minimizes recombination losses, which leads to better performance. As an HTL, the CBTS offers excellent stability and improved hole transport. The synergy between IGZO ETL and CBTS HTL results in a low recombination with high charge transport, providing the best photovoltaic efficiency with the total highest PCE in all tested combinations. Fig. 3(f) demonstrates that C$_{60}$ as ETL with CBTS as HTL provide the lowest PCE of 21.57% (V_{oc} = 1.240 V, J_{sc} = 19.957 mA cm^{-2}, and FF = 87.11%). C$_{60}$ has reasonable electron transport, but its higher electron mobility than other ETLs leads to the lowest efficiency. While the CBTS is still effective as an HTL, the overall device performance is limited by the reduced electron extraction efficiency of C$_{60}$. IGZO ETL + CBTS HTL has the highest PCE among all combinations, exceeding 23.90% in the most optimum conditions, thus qualifying as the best performing pair. Thus, the high electron mobility, excellent energy-level alignment and chemical stability of IGZO lead to superior electron extraction, while CBTS provides efficient hole collection with minimal recombination losses. This combination optimizes both charge separation as well as charge transport, yielding the highest overall efficiency.[49,50]

3.2.2. Selection of ETL and HTL for Rb$_2$AuScCl$_6$-based solar cells. Fig. 4(a) depicts the optimal performance of 20.99% PCE of WS$_2$ ETL/CBTS HTL is obtained with V_{oc}, J_{sc}, FF of 1.447 V, 16.289 mA cm^{-2}, and 89.04% respectively. The high electron mobility of WS$_2$, together with good alignment of its energy levels with the perovskite material, gives better electron extraction than TiO$_2$ and ZnO. These also match well with CBTS, which provides ideal hole transport; thus, the pair yields the highest PCE attributed to ideal transport properties of both electrons and holes, resulting in minimized recombination and maximized efficiency during transport. Fig. 4(b) illustrates that when use ZnO as ETL with CBTS as HTL (PCE = 20.21% V_{oc} = 1.451 V, 15.659 mA cm^{-2}, 88.92% FF). Though ZnO has excellent electron transport layer properties, its performance is slightly less favorable than WS$_2$ due to slight differences in the energy level alignment and a lower electron mobility than WS$_2$, yielding a slightly lower PCE. Fig. 4(c) shows PCE reaches 19.68% with this structure obtained by ETL of PCBM and HTL of CBTS, while showing V_{oc} of 1.401 V, J_{sc} of 15.634 mA cm^{-2} and FF of 89.84%. While PCBM is known to be a good electron acceptor, the relatively lower mobility of electrons compared to WS$_2$ and ZnO results in a slight decrease in PCE value. Assure that the fill factor is high, the net efficiency is reduced by a factor of lower electron mobility. While the configuration of

TiO$_2$ ETL and CBTS HTL enables a PCE of 20.33% (V_{oc} = 1.452 V, J_{sc} = 15.659 mA cm^{-2}, and FF = 89.41%) (Fig. 4(d)). This arrangement strikes a good trade-off between the extraction of electrons and collection of holes, and thus their resulting performance is moderate, whereas the material characteristics of TiO$_2$ do not allow for the most optimal conversion efficiency. In Fig. 4(e) achieves PCE of 19.04% with V_{oc}, J_{sc}, FF of 1.416 V, 15.657 mA cm^{-2}, 85.85% respectively using IGZO as ETL and CBTS as HTL combination. IGZO possesses high electron mobility yet is somewhat less efficient than WS$_2$ and ZnO, which is likely a result of interface effects and energy level mismatches with the perovskite layer. This means that despite IGZO's electron mobility, the performance is not as good. Fig. 4(f) depicts the composition of C$_{60}$ ETL and CBTS HTL gives the lowest PCE of 16.51%, with V_{oc} of 1.266 V, J_{sc} of 14.888 mA cm^{-2}, and FF of 87.61%. While C$_{60}$ offers decent electron transport, its lower electron mobility compared to the other ETLs results in the overall lowest device efficiency. CBTS is efficient as the HTL, but its reduced electron mobility hampers performance.[51]

3.3. Role of absorber thickness and ETL thickness on solar cell performance

Fig. 5 demonstrates a series of contour plots showing the PCE of perovskite solar cells. We are testing various materials as the ETL, while using Rb$_2$AuScBr$_6$ as the perovskite absorber material. Each sub-figure (a–f) represents a different ETL configuration.

Fig. 5(a) shows the PCE achieved is around 21.80% when C$_{60}$ is used as the ETL. The contour lines indicate how the PCE changes with varying thicknesses of both the absorber and the C$_{60}$ ETL. Fig. 5(b) demonstrates that using Indium Gallium Zinc Oxide (IGZO) as the ETL results in the highest PCE of 24.07%. The contour lines are more spread out compared to C$_{60}$, suggesting a wider range of thicknesses for both the absorber and IGZO that yield high efficiency. This indicates that the performance is less sensitive to small variations in the thicknesses. Fig. 5(c) illustrates the use of PCBM as the ETL, achieving a peak PCE of approximately 23.80%. The optimal performance region appears to be in the lower left corner, implying that thinner layers of both the absorber and PCBM are generally preferred for maximizing efficiency in this configuration. Fig. 5(d) shows that using WS$_2$ is the ETL reaches PCE is approximately 23.91%. Similar to PCBM, the optimal performance seems to be achieved with thinner layers, as indicated by the concentration of contour lines in the lower-left region. From Fig. 5(a–d) the highest PCE of absorber thicknesses is ≥1200 nm and ETL thicknesses are ≤50 nm. Fig. 5(e) employs titanium dioxide (TiO$_2$) as the ETL and achieves a comparable peak PCE of approximately 23.87%, where the optimal condition is observed at absorber thicknesses ≥1200 nm and an ETL thickness precisely at 200 nm. The contour lines are closely packed, suggesting a narrow region of high efficiency. This implies that the performance is quite sensitive to the thicknesses of both the absorber and TiO$_2$, and precise control is crucial. Fig. 5(f) demonstrates that Zinc Oxide (ZnO) is the ETL, and peak PCE is about 23.88%. Where absorber thicknesses are ≥1200 nm and

ETL thicknesses are 450 nm. Like TiO_2, the contour plot indicates a narrow region of high efficiency and thus sensitivity to thickness variations.

The superior PCE of IGZO is mainly attributed to its favorable energy band alignment with the $Rb_2AuScBr_6$ absorber, which enables electron extraction and prevents the leakage of
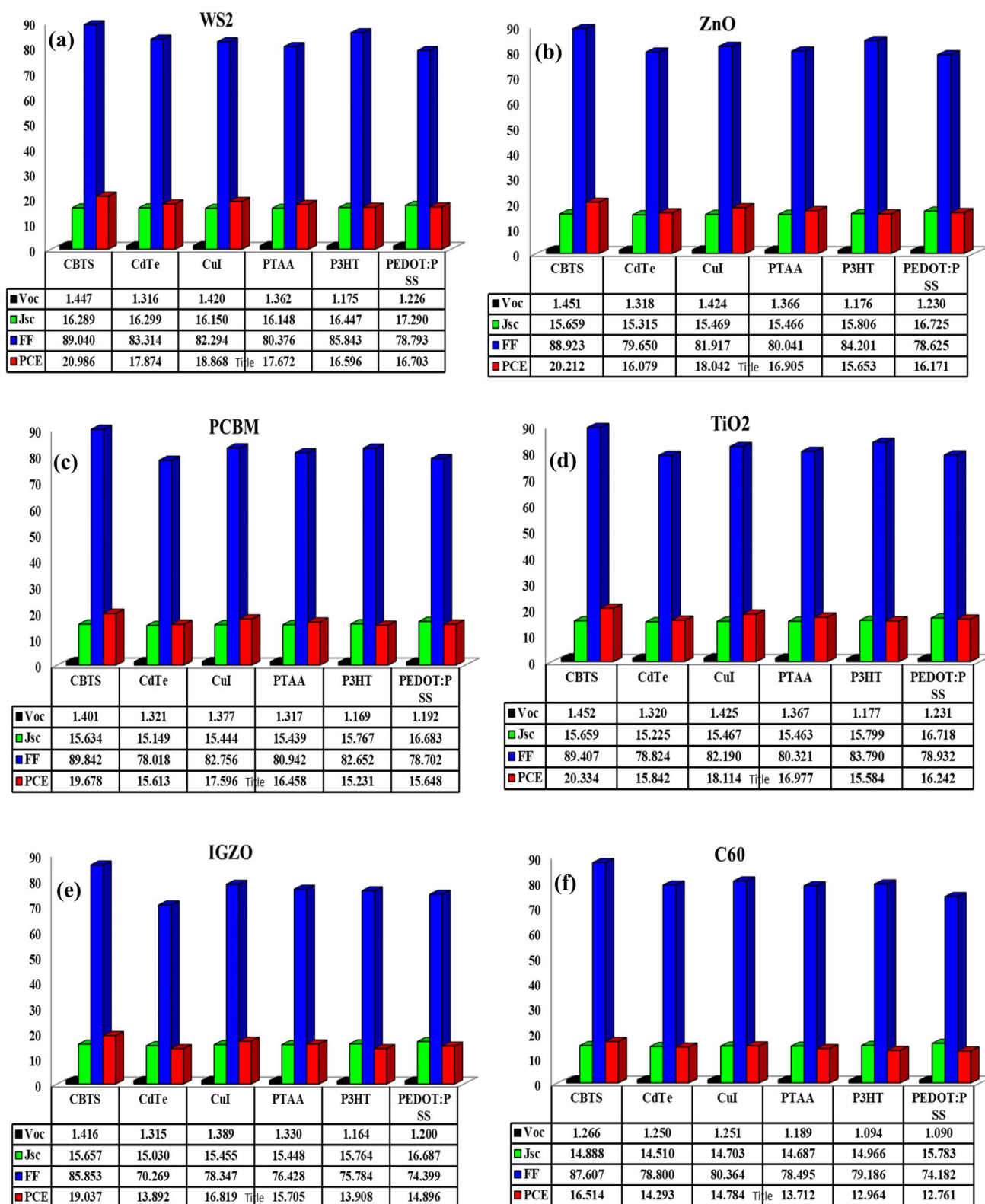
WS2 (a)

	CBTS	CdTe	CuI	PTAA	P3HT	PEDOT:PSS
Voc	1.447	1.316	1.420	1.362	1.175	1.226
Jsc	16.289	16.299	16.150	16.148	16.447	17.290
FF	89.040	83.314	82.294	80.376	85.843	78.793
PCE	20.986	17.874	18.868	17.672	16.596	16.703

ZnO (b)

	CBTS	CdTe	CuI	PTAA	P3HT	PEDOT:PSS
Voc	1.451	1.318	1.424	1.366	1.176	1.230
Jsc	15.659	15.315	15.469	15.466	15.806	16.725
FF	88.923	79.650	81.917	80.041	84.201	78.625
PCE	20.212	16.079	18.042	16.905	15.653	16.171

PCBM (c)

	CBTS	CdTe	CuI	PTAA	P3HT	PEDOT:PSS
Voc	1.401	1.321	1.377	1.317	1.169	1.192
Jsc	15.634	15.149	15.444	15.439	15.767	16.683
FF	89.842	78.018	82.756	80.942	82.652	78.702
PCE	19.678	15.613	17.596	16.458	15.231	15.648

TiO2 (d)

	CBTS	CdTe	CuI	PTAA	P3HT	PEDOT:PSS
Voc	1.452	1.320	1.425	1.367	1.177	1.231
Jsc	15.659	15.225	15.467	15.463	15.799	16.718
FF	89.407	78.824	82.190	80.321	83.790	78.932
PCE	20.334	15.842	18.114	16.977	15.584	16.242

IGZO (e)

	CBTS	CdTe	CuI	PTAA	P3HT	PEDOT:PSS
Voc	1.416	1.315	1.389	1.330	1.164	1.200
Jsc	15.657	15.030	15.455	15.448	15.764	16.687
FF	85.853	70.269	78.347	76.428	75.784	74.399
PCE	19.037	13.892	16.819	15.705	13.908	14.896

C60 (f)

	CBTS	CdTe	CuI	PTAA	P3HT	PEDOT:PSS
Voc	1.266	1.250	1.251	1.189	1.094	1.090
Jsc	14.888	14.510	14.703	14.687	14.966	15.783
FF	87.607	78.800	80.364	78.495	79.186	74.182
PCE	16.514	14.293	14.784	13.712	12.964	12.761

Fig. 4 HTL & ETL Selection for $Rb_2AuScCl_6$ of (a) Ws_2 (b) ZnO (c) PCBM, (d) TiO_2, (e) IGZO and (f) C_{60} with HTL of CBTS, CdTe, CuI, PTAA, P3HT and PEDOT : PSS.

Fig. 5 Contour mapping of PCE, when the absorber is Rb$_2$AuScBr$_6$ and ETLs as (a) C$_{60}$. (b) IGZO, (c) PCBM, (d) WS$_2$, (e) TiO$_2$ and (f) ZnO.

holes into the ETL. Moreover, the high electron mobility of IGZO decreases recombination losses by quickly transporting charge carriers to the contact. The wide thickness tolerance (shown as contours that are further apart) means that even with small variations in the thickness of the absorber or ETL layer high efficiency can be obtained. This upon favorable band

alignment, fast charge transport, and thickness-independence, which altogether result in the superior device performances of IGZO. Fig. 6 shows how the PCE of perovskite solar cells changes when using different electron transport layers (ETLs) with the perovskite material Rb$_2$AuScCl$_6$. Each of the six sub-figures (a–f) represents a different ETL. Fig. 6(a) (C$_{60}$ ETL)

Fig. 6 Contour mapping of PCE when absorber is Rb_2ScCl_6 and ETLs as (a) C_{60}, (b) IGZO, (c) PCBM, (d) WS_2, (e) TiO_2 and (f) ZnO.

shows a maximum PCE of 16.65%. Where absorber thicknesses are ≥1000 nm and ETL thicknesses are ≤50 nm. The contour lines are relatively spread out, suggesting a less critical dependence on precise thickness control compared to some other

ETLs. Fig. 6(b) (IGZO ETL) exhibits a significantly higher maximum PCE, reaching approximately 18.96%. Where absorber thicknesses are ≥1500 nm and ETL thicknesses are ≤450 nm. The high PCE region is broad, indicating good

tolerance to variations in both absorber and ETL thicknesses. Fig. 6(c) (PCBM ETL) achieves a maximum PCE around 19.80%. The optimal performance seems to be associated with a specific range of thicknesses, as indicated by the concentrated contour lines. Fig. 6(d) (WS$_2$ ETL) shows a maximum PCE of about 22.76%. This is the highest PCE among the tested ETLs in this figure. The contour plot suggests a well-defined region of optimal performance. From the Fig. 6(c) and (d) reveal that the highest PCEs are achieved when the absorber thicknesses are $\geq$1200 nm and ETL thicknesses are $\leq$50 nm. Fig. 6(e) (TiO$_2$ ETL) reaches a maximum PCE of approximately 20.41% when absorber thicknesses are equal to 1200 nm and ETL thicknesses are less than or equal to 50 nm. Fig. 6(f) (ZnO ETL) exhibits a maximum PCE of 20.30% where the thicknesses are equal to 1400 nm and ETL thicknesses are equal to 450 nm. Based on Fig. 6, WS$_2$ is the best-performing ETL layer, achieving the highest maximum PCE of approximately 22.76%. This suggests that WS$_2$, in combination with the Rb$_2$ScCl$_6$ perovskite absorber, facilitates the most efficient charge transfer and transport among the materials tested. WS$_2$ performs best because its energy band alignment with the Rb$_2$AuScCl$_6$ absorber is optimal for efficient electron extraction. Its conduction band level is ideally positioned to collect electrons while preventing hole injection, thereby reducing recombination losses. Additionally, WS$_2$'s high electron mobility and layered structure facilitate rapid charge transport, ensuring that the generated carriers are efficiently transferred through the device, which in turn maximizes the power conversion efficiency.[52]

3.4. Impact of absorber thickness with best ETL

Absorber thickness had a large impact on the performance of ITO/ETL/Rb$_2$AuScBr$_6$/CBTS/Ni and ITO/ETL/Rb$_2$AuScCl$_6$/CBTS/Ni structures. The absorber thickness was varied from 400 nm to 2000 nm to improve the efficiency of devices and the effect has been studied on performance parameters. All the results obtained in the PSC showed that the V_{oc} tended to decrease as the absorber thickness increased. This drop is accompanied by the increase of reverse saturation current, resulting in charge recombination losses.[53,54] The Rb$_2$AuScBr$_6$-based device exhibited a decrease in V_{oc} from 1.299 V at 400 nm to 1.25 V at

2000 nm; however, Rb$_2$AuScCl$_6$ remained at a more stable V_{oc} of 1.44–1.46 V. As illustrated in Fig. 7(a) J_{sc} increased as a result of improved light absorption with increasing absorber thickness. This trend is explained by the better spectral response at longer wavelengths for thicker absorbers. The J_{sc} increased from 18.46 mA cm^{-2} (400 nm) to 21.87 mA cm^{-2} (2000 nm) for the Rb$_2$AuScBr$_6$-based structure and from 15.65 mA cm^{-2} (600 nm) to 16.46 mA cm^{-2} (2000 nm for the Rb$_2$AuScCl$_6$).

In Fig. 7(b), the Rb$_2$AuScBr$_6$-based device exhibited FF of up to 88.4–88.5%, while that of Rb$_2$AuScCl$_6$ stayed constant at 88.4–89.1%. With respect to power conversion efficiency (PCE), both materials exhibit an increase in PCE with increasing absorber thickness, peaking and subsequently declining slightly due to recombination losses.

For Rb$_2$AuScBr$_6$, the highest was 24.08% at 2000 nm, and Rb$_2$AuScCl$_6$ reached 21.07% at 1600 nm. Although an optimized absorber thickness of 1600 nm for both Rb$_2$AuScBr$_6$ and R$_2$AuScCl$_6$ results in the highest device performance, a thinner absorber layer is generally more desirable for perovskite solar cells (PSCs).[55] Therefore, an absorber thickness of 1200 nm was selected as the optimal design choice for this study.

3.5. Influence of metal back contact on solar cell performance

Fig. 8 illustrates the influence of the metal back contact's work function (WF) on key performance parameters V_{oc}, (J_{sc}), PCE, and FF for two device configurations: ITO/IGZO/Rb$_2$AuScBr$_6$/CBTS/Metal and ITO/WS$_2$/Rb$_2$AuScCl$_6$/CBTS/Metal. In the case of the Rb$_2$AuScBr$_6$-based device, the highest performance is achieved with a work function of 5.5 eV, where the device exhibits a V_{oc} of 1.36 V, J_{sc} of 21.42 mA cm^{-2}, FF of 87.14%, and a maximum PCE of 25.3%. Notably, enhancing the work function beyond 5.5 eV does not significantly affect the PCE, indicating stability in device performance. Due to this optimized performance and the favorable alignment with the Ni back contact (WF = 5.5 eV), nickel is selected as the preferred back electrode for this device. For the Rb$_2$AuScCl$_6$-based device, the highest PCE of 22.48% is observed at a work function of 5.8 eV, with corresponding values of V_{oc} = 1.53 V, J_{sc} = 16.15 mA cm^{-2}, and FF = 90.78%.
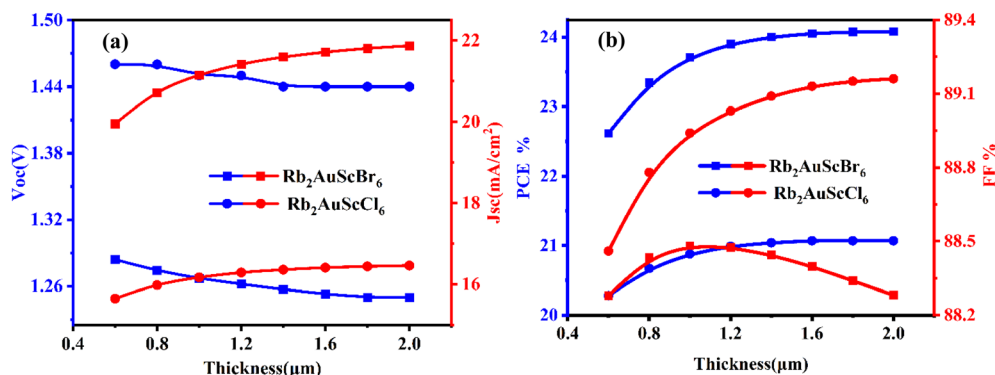

Fig. 7 Effect of absorber thickness on performance parameters (a) V_{oc}, and J_{sc}, (b) PCE and FF of (ITO/IGZO/Rb$_2$AuScBr$_6$/CBTS/Ni) (ITO/WS$_2$/Rb$_2$AuScCl$_6$/CBTS/Ni) devices.
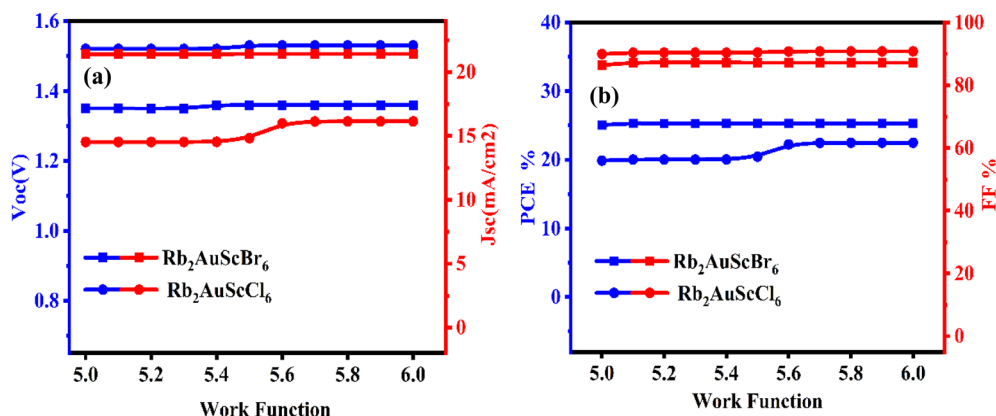
Fig. 8 Effect of Metal Back Contact on performance parameters (a) V_{oc}, and J_{sc}, (b) PCE and FF of (ITO/IGZO/Rb$_2$AuScBr$_6$/CBTS/Ni) (ITO/WS$_2$/Rb$_2$AuScCl$_6$/CBTS/Ni) devices.

However, metals with a work function of 5.8 eV, such as platinum (Pt), are highly expensive and thus less viable for commercial use. Therefore, nickel (WF = 5.5 eV) is adopted as a cost-effective alternative. With Ni as the back contact, the device still demonstrates respectable performance, achieving a PCE of 20.45%, V_{oc} of 1.53 V, J_{sc} of 14.83 mA cm^{-2}, and FF of 90.43%.

In summary, the feasibility and cost-effectiveness of using nickel as the back contact support its selection for both device architectures.[56]

3.6. Effect of acceptor density on the solar cell PCE

The impact of acceptor density on PCE has been analyzed for two device architectures: ITO/IGZO/Rb$_2$AuScBr$_6$/CBTS/Ni and ITO/WS$_2$/Rb$_2$AuScCl$_6$/CBTS/Ni. Fig. 9 illustrates variations in V_{oc}, J_{sc}, FF, and PCE as functions of acceptor density, highlighting efficiency trends in both configurations. From Fig. 9(b), PCE follows a similar trend with the increase of acceptor density, reaches a maximum value, and then decreases steadily. The maximum value of PCE (25.81%) occurs for the Rb$_2$-AuScBr$_6$-based device with an acceptor density of 10^{18} cm^{-3}, at V_{oc} = 1.37 V, J_{sc} = 21.26 mA cm^{-2}, and FF = 88.94%. Likewise,

the Rb$_2$AuScCl$_6$-based device exhibits a maximum PCE of 22.41% at the acceptor density of 10^{17} cm^{-3}, at V_{oc} = 1.53 V, J_{sc} = 16.16 mA cm^{-2}, and FF = 90.65%, after which the efficiency drops. The increase in V_{oc} may be attributed to the increased charge carrier separation due to increased internal electric field as a result of increased acceptor density.

Increase in doping concentration contributes to a reduction in series resistance (as such, improving FF) and a reduction in surface recombination losses. In contrast with V_{oc} and FF, J_{sc} is almost unchanged, suggesting that the doping variations have little impact on light absorption and carrier generation. The results highlight the critical role of optimizing acceptor density in enhancing solar cell efficiency. Among the studied devices, Rb$_2$AuScBr$_6$-based solar cells demonstrated superior performance compared to Rb$_2$AuScCl$_6$ counterparts, which can be attributed to their improved charge transport characteristics and more favorable optical properties.

3.7. Influence of absorber defect density on solar cell behavior

The value of defect density (N_t) in the absorber layer has a great impact on the overall efficiency of solar cell devices.[57] Fig. 10(a)
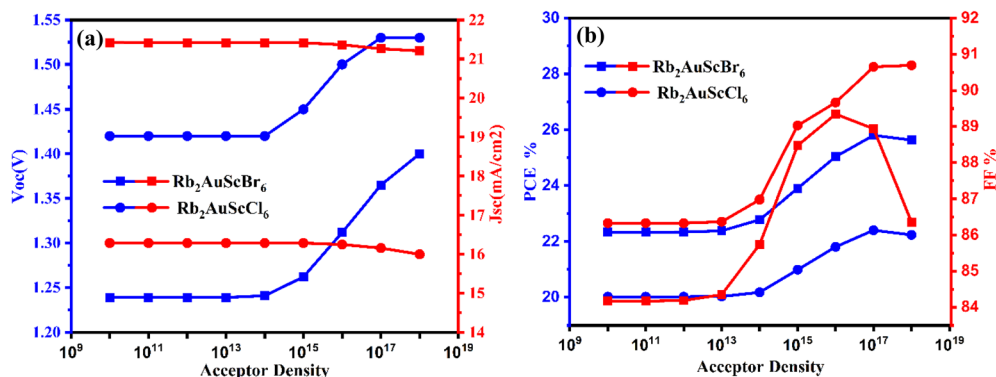

Fig. 9 Variation of cell parameters with changing acceptor density (a) V_{oc} and J_{sc}, (b) PCE and FF of (ITO/IGZO/Rb$_2$AuScBr$_6$/CBTS/Ni) and (ITO/WS$_2$/Rb$_2$AuScCl$_6$/CBTS/Ni) devices.
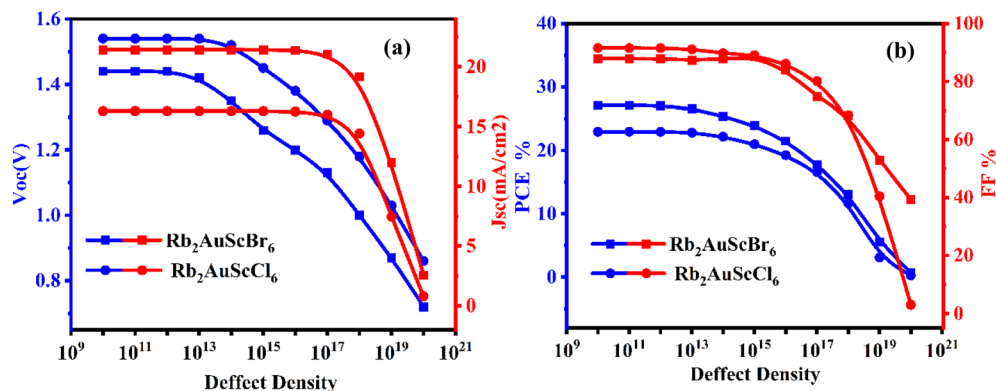
Fig. 10 Effect of absorber defect density (N_t) on performance parameters (a) V_{oc} and J_{sc}, (b) PCE and FF of (ITO/IGZO/Rb$_2$AuScBr$_6$/CBTS/Ni) (ITO/WS$_2$/Rb$_2$AuScCl$_6$/CBTS/Ni) devices.

and (b) of devices based on Rb$_2$AuScBr$_6$ and Rb$_2$AuScCl$_6$, respectively. The characteristic of increasing N_t leads to the reduction of V_{oc}, J_{sc}, FF, and PCE in both devices. Under these conditions, the best PCE of 27.11% can be obtained for the Rb$_2$AuScBr$_6$-based device with the parameters of $V_{oc} = 1.44$ V, $J_{sc} = 21.42$ mA cm^{-2}, and FF = 87.88%. This high efficiency is maintained when the defect density in the absorber layer is at 10^{10} cm^{-3}. In a similar, the Rb$_2$AuScCl$_6$-based device reaches its highest PCE = 22.96% with $V_{oc} = 1.54$ V, $J_{sc} = 16.29$ mA cm^{-2}, and FF = 91.53%.

Although the highest PCEs of 27.11% for the Rb$_2$AuScBr$_6$-based absorber and 22.96% for the Rb$_2$AuScCl$_6$-based absorber were obtained at a defect density of 10^{10} cm^{-3}, such a low defect density is not considered realistic or acceptable. In practical conditions, the defect density cannot be reduced below 10^{14} cm^{-3} and must at least be maintained at this level. At a more acceptable defect density of 10^{15} cm^{-3},[58] the Rb$_2$AuScBr$_6$-based absorber achieves a PCE of 23.90%, while the Rb$_2$AuScCl$_6$-based absorber reaches a PCE of 20.99%.

3.8. Influences of electron affinity on solar cell behavior

Solar cell efficiency is influenced by the electron affinity of the absorber layer. Fig. 11(a) and (b) depict the variations of V_{oc}, J_{sc},

FF, and PCE with electron affinity for the Rb$_2$AuScBr$_6$ and Rb$_2$AuScCl$_6$-based devices, respectively.

For the Rb$_2$AuScBr$_6$-based device, the optimal electron affinity (3.95) eV, producing the maximum PCE of 23.12% with $V_{oc} = 1.26$ V, $J_{sc} = 21.41$ mA cm^{-2}, and FF = 88.65%. When the electron affinity becomes larger than this optimal value, the efficiency declines due to a band misalignment, with a corresponding loss of V_{oc} and FF. However, with further increasing EA at 4.50 eV, PCE decreases sharply to 15.93%, highlighting the negative influences of excessive electron affinity on carrier extraction.

For the device based on Rb$_2$AuScCl$_6$, the peak PCE of 21.06% is achieved at 3.70 eV, with $V_{oc} = 1.45$ V, $J_{sc} = 16.29$ mA cm^{-2}, and FF = 88.94%. Above this region, the efficiency begins to decrease, with a serious drop at 4.30 eV and 4.50 eV, with the value of PCE being as low as 8.54% and 6.33%, respectively. The diminished performance at increased electron affinity can be attributed to larger recombination losses and diminished built-in potential, which compromise charge separation and collection efficiency. Thus, tuning the electron affinity for the absorber is crucial for achieving higher cell efficiency. These findings confirm that Rb$_2$AuScBr$_6$ is indeed a better candidate for the development of efficient devices than Rb$_2$AuScCl$_6$, because its superior electrical properties allow for boosting charge transport and decreasing recombination losses.
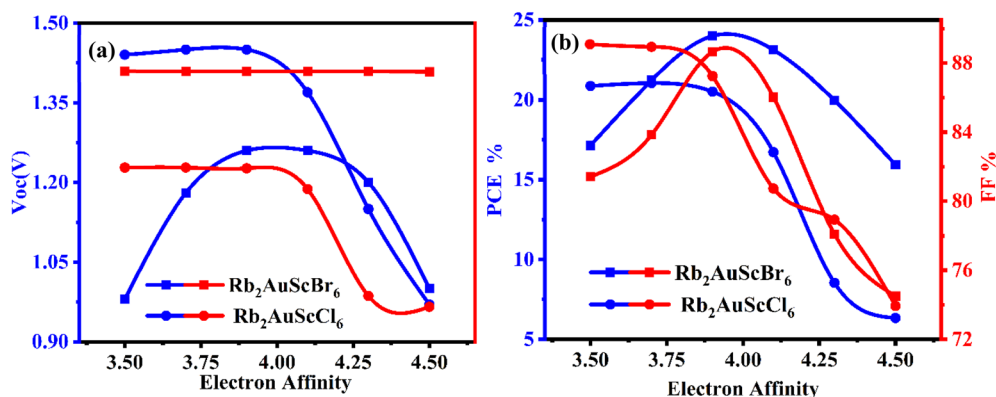

Fig. 11 Effect of absorber electron affinity on performance parameters (a) V_{oc} and J_{sc}, (b) PCE and FF of (ITO/IGZO/Rb$_2$AuScBr$_6$/CBTS/Ni) (ITO/WS$_2$/Rb$_2$AuScCl$_6$/CBTS/Ni) devices.

This improvement can be attributed to the better light intensity of $Rb_2AuScBr_6$ caused by the optimal band gap, which leads to better light absorption and efficient excitation of charge carriers.[59,60] It achieves a better conduction-band alignment to maintain a matched band gap, improving the tandems V_{oc}, J_{sc}, and FF balance, and therefore higher efficiencies are obtained than for $Rb_2AuScCl_6$. To put it plainly, $Rb_2AuScBr_6$ is more efficient at absorbing light, produces a lot of more beneficial charge carriers, and minimizes energy losses, which all contribute to it being better suited for high-performance solar cells.

3.9. Influences of electron mobility on solar cell performance

In contrast, the power conversion efficiency (PCE) exhibits a slight upward trend, particularly at lower μ_e values. For $Rb_2AuScCl_6$, the PCE increases from 20.73% to 21.00% as μ_e reaches 90 cm^2 V^{-1} s^{-1}, while for $Rb_2AuScBr_6$, it rises from 23.00% to 23.92% within the same range. This improvement is attributed to enhanced charge-transport capability, reduced series resistance, and suppression of electron accumulation at interfaces, which collectively lower recombination losses and improve carrier extraction.

Fig. 12(a) and (b) shows the effect of electron mobility (μ_e) in the range of 10–100 cm^2 V^{-1} s^{-1} on the photovoltaic performance of $Rb_2AuScCl_6$-and $Rb_2AuScBr_6$-based perovskite solar cells. The short-circuit current density (J_{sc}) and open-circuit voltage (V_{oc}) remain largely unchanged with increasing μ_e, indicating stable charge generation and extraction across the studied mobility range.

As μ_e approaches 90 cm^2 V^{-1} s^{-1}, the PCE reaches a near-saturation region, indicating that carrier transport becomes sufficiently efficient and further mobility enhancement yields minimal benefit. Beyond this point, the device performance is primarily limited by interfacial recombination, optical absorption constraints, and hole-transport efficiency rather than electron mobility alone.

Overall, electron mobility has a positive yet bounded influence on device performance.[61] An optimal mobility window of 80–90 cm^2 V^{-1} s^{-1} ensures maximum PCE, beyond which additional increases in μ_e do not result in notable efficiency gains.

3.10. Effect of series resistance (R_s) on solar cell performance

The effect of R_s (series resistance) is a significant factor in solar cell efficiency. R_s was varied from 1 Ω to 8 Ω cm^2 in order to investigate its effect on output parameters while maintaining shunt resistance (R_{sh}) constant at a value of 10^5 Ω cm^2, as shown in Fig. 13(a) and (b). J_{sc}, on the other hand, is relatively insensitive to series resistance; J_{sc} remains almost unchanged, but V_{oc} and FF gradually decrease as R_s increases due to more significant resistive losses.[62] For devices based on $Rb_2AuScBr_6$, the maximum PCE of 23.90% is achieved with $R_s = 1$ Ω, $V_{oc} = 1.26$ V, $J_{sc} = 21.41$ mA cm^{-2}, and FF = 88.48%. In a similar trend for $Rb_2AuScCl_6$-based devices, a maximum PCE of 20.99% occurs at $R_s = 1$ Ω ($V_{oc} = 1.45$ V, $J_{sc} = 16.29$ mA cm^{-2}, and FF = 89.03%). With higher R_s, PCE decreases due to a fall in FF and a small decrease in V_{oc}. The increased resistive losses and suppressed charge transport caused by a higher R_s result in larger resistive losses and lower power output. Nevertheless, $Rb_2AuScBr_6$-based devices show higher PCE than their $Rb_2AuScCl_6$ counterparts, revealing better charge carrier mobility and reduced recombination losses.[63,64] We found that reducing R_s is critical for improving solar cell performance, as lower resistance in series leads to better efficiency and improved charge extraction.[65] Additionally, a higher R_s increases the voltage drop across the device under forward bias, which limits the charge extraction capability and accelerates recombination within the absorber and interfaces. This results in diminished diode quality and reduced operational stability, particularly under high-intensity illumination or prolonged operation. Therefore, maintaining a low R_s is essential not only for maximizing PCE but also for ensuring long-term device reliability and efficient carrier transport pathways.

3.11. Effect of shunt resistance (R_{sh}) on solar cell performance

Shunt resistance (R_{sh}) is an important parameter for the overall performance of perovskite solar cells (PSCs). Low R_{sh} causes power losses mainly resulting from leakage current and non-geminate recombination losses. These losses happen due to partial junction shorts that arise from pinholes and metal filling
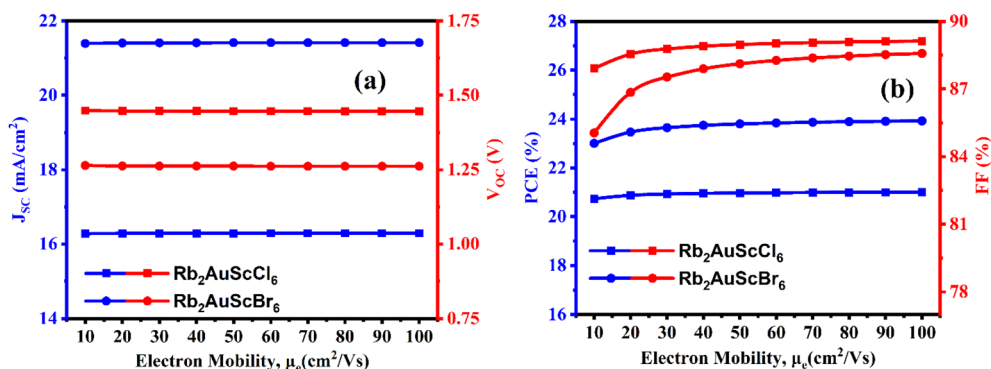

Fig. 12 Effect of absorber electron mobility on performance parameters (a) V_{oc} and J_{sc}, (b) PCE and FF of (ITO/IGZO/$Rb_2AuScBr_6$/CBTS/Ni) (ITO/WS_2/$Rb_2AuScCl_6$/CBTS/Ni) devices.
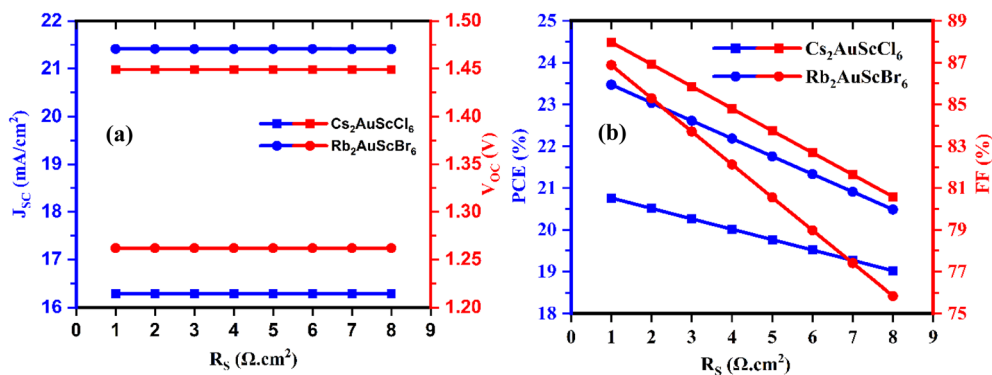
Fig. 13 Effect of series resistance (R_s) on performance parameters (a) V_{oc} and J_{sc}, (b) PCE and FF of (ITO/IGZO/Rb$_2$AuScBr$_6$/CBTS/Ni) (ITO/WS$_2$/Rb$_2$AuScCl$_6$/CBTS/Ni) devices.

reaching the junctions. In this case, low R_{sh} (parallel resistance) allows for a bypass of the solar cell itself and hence reduces voltage (V_{oc}) and calculated current flow through the junction. R_{sh} plays a more important role at low light due to the contribution of current loss being dominant when the light-generated current is already at low levels.[66,67] To reduce these losses, a variety of techniques have been employed to increase R_{sh}, such as doping the ETL with lead (Pb) to increase resistance further. The R_{sh} value can be, therefore, conveniently amended for making good device efficiency when the Pb content is carefully adjusted. V_{oc}, J_{sc}, FF, and PCE are analyzed for Rb$_2$AuScBr$_6$ and Rb$_2$AuScCl$_6$-based solar cells—keeping R_{sh} in the range of 10 to 10^8 Ω, while R_S was fixed throughout at 1 Ω cm^2.

The data are summarized in Fig. 14(a) and (b). The maximum PCE of Rb$_2$AuScBr$_6$-based devices reached 23.90% at $R_{sh} = 10^6$ Ω, with $V_{oc} = 1.26$ V, $J_{sc} = 21.41$ mA cm^{-2}, and FF = 88.48%. In the same manner, for Rb$_2$AuScCl$_6$-based devices, 20.99% of the maximum PCE occurs at $R_{sh} = 10^7$ Ω, with $V_{oc} = 1.45$ V, $J_{sc} = 16.29$ mA cm^{-2} and FF = 89.03%. With the increase of R_{sh}, V_{oc} and FF is effectively increased, significantly improving the PCE. But it plateaus above 10^6 Ω (Rb$_2$AuScBr$_6$) and 10^7 Ω (Rb$_2$AuScCl$_6$), demonstrating that additional increases in R_{sh} have an insignificant influence on performance.

These data underscore that R_{sh} is important for optimizing PSC efficiency. High R_{sh} ($\geq10^4$ Ω) is crucial for reducing leakage

currents and recombination losses to guarantee better charge collection and enhanced device performance.[68,69] The improved performance seen in Rb$_2$AuScBr$_6$-based devices demonstrates that with higher charge transport ability and minimized recombination losses, Rb$_2$AuScBr$_6$-based devices can outperform their Rb$_2$AuScCl$_6$ analogs. For further insights to better understand the behavior of R_{sh} and R_s, an ideal single-diode model has been described using eqn (11).

$$I = I_L - I_0\left[\exp\left(\frac{q(M)}{Ak_BT}\right) - 1\right] - \frac{M}{R_{sh}} \quad (11)$$

where A stands for ideality factor, k_B for Boltzmann constant, T for temperature, q for electron charge, and $M = V + (I \times R_s)$. The opposite saturation current of the diode is I_0, while the light-induced current is I_L. Eqn (12) and (13) are the R_s and R_{sh} equations, respectively, derived from the J–V curves, in which ΔV stands for voltage change and ΔI for current change.

$$R_{sh} = -\frac{\Delta V}{\Delta I}(V = 0) \quad (12)$$

$$R_s = -\frac{\Delta V}{\Delta I}(V = V_0) \quad (13)$$

As described in eqn (11), the term $\frac{M}{R_{sh}}$ represents the parasitic leakage current path, meaning that a lower R_{sh} increases
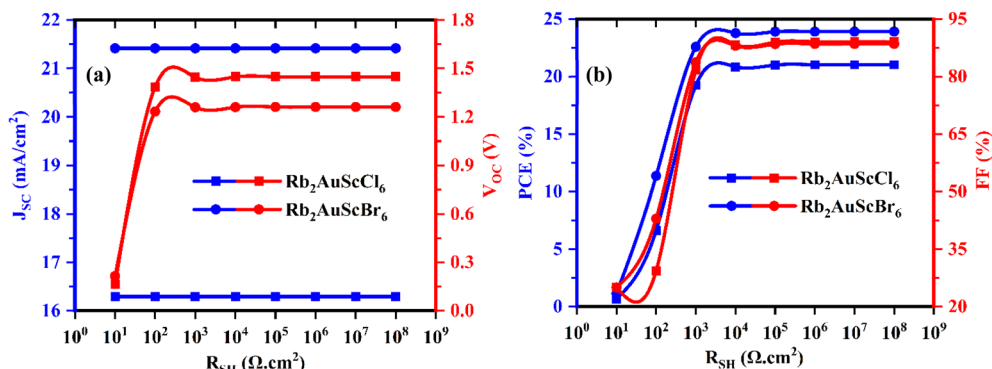

Fig. 14 Effect of shunt resistance (R_{sh}) on performance parameters (a) V_{oc} and J_{sc}, (b) PCE and FF of (ITO/IGZO/Rb$_2$AuScBr$_6$/CBTS/Ni) (ITO/WS$_2$/Rb$_2$AuScCl$_6$/CBTS/Ni) devices.

the portion of current that bypasses the junction, thereby reducing the net photocurrent and weakening the diode characteristics. When R_{sh} is sufficiently high, this leakage component becomes negligible, ensuring efficient charge extraction and sustaining higher V_{oc} and FF. Therefore, maintaining a large R_{sh} is critical for suppressing shunt-induced recombination losses and achieving ideal diode behavior and superior device performance.

3.12. Role of temperature on solar cell performance

Temperature causes a large change in V_{oc}, J_{sc}, FF, and PCE of PSCs, influencing the efficiency of PSCs. A high temperature can cause V_{oc} and FF to drop, leading to a corresponding drop in PCE. This decrease is due to increased recombination of charge carriers, thermally activated effects, and changes in material properties that limit device performance. In PSCs, J_{sc} shows almost no temperature dependence, revealing that the absorption properties of the absorber layers are not affected by the temperature.[70] The temperature (300–440 K) effects on V_{oc}, J_{sc}, FF, and PCE of both Rb$_2$AuScBr$_6$ and Rb$_2$AuScCl$_6$-based solar cells are presented in Fig. 14(a) and (b). The maximum PCE of Rb$_2$AuScBr$_6$-based devices is up to 23.901% at 300 K with V_{oc} = 1.262 V, J_{sc} = 21.41 mA cm^{-2}, and FF = 88.475%. Likewise, the PCE of Rb$_2$AuScCl$_6$-based devices is 21.013% at 300 K, with V_{oc} = 1.449 V, J_{sc} = 16.289 mA cm^{-2}, and FF = 89.036%. This ensures a negative impact of higher temperatures on the solar cell performance, as well as a positive impact of lower operating temperature on efficiency.[71]

3.13. Impact of capacitance, Mott–Schottky, generation and recombination rate

The C–V behavior of Rb$_2$AuScBr$_6$ and Rb$_2$AuScCl$_6$-based PSCs is shown in Fig. 15(a) An increased capacitance with voltage indicates charge accumulation at the interface. Capacitance for Rb$_2$AuScBr$_6$ is much higher than Rb$_2$AuScCl$_6$, suggesting a larger charge storage capability of Rb$_2$AuScCl$_6$ along with enhanced charge carrier density. This implies that Rb$_2$AuScCl$_6$ possesses enhanced dielectric behavior and more efficient charge transport, factors that may be responsible for its corresponding higher power conversion efficiency (PCE). The

junction capacitance per area was determined using a known relation:[72]

$$\frac{1}{C^2} = \frac{2\varepsilon_0 \varepsilon_r}{q N_d}(V_{bi} - V) \tag{14}$$

where ε_0 is vacuum permittivity, ε_r is the dielectric constant, q is electronic charge, and A is the area of the device. The value of N_d is derived from the gradient of the linear region in the M–S plot, while V_{bi} is the extrapolated segment from the linear segment to the voltage axis.

As seen in Fig. 16(b), the Mott–Schottky plot ($1/C^2$ vs. Voltage) shows that the equation gives the information on the built-in potential and the carrier density. The flatter slope in the Rb$_2$AuScCl$_6$ device corresponds to higher N_d, which improves the internal electric field distribution, leading to better carrier transport and reduced recombination losses. Notably, the built-in potential V is higher in the Rb$_2$AuScBr$_6$ cell, supporting stronger band bending and more efficient charge separation at the junction. Fig. 16(c) and (d) demonstrate the spatial profiles of the carrier generation and recombination rates within both device structures. The generation rate profile reveals that Rb$_2$AuScBr$_6$-based cells exhibit a peak carrier generation rate of ~10^{22} cm^{-3} s^{-1}, slightly exceeding that of the Rb$_2$AuScCl$_6$-based cells, which peak around ~10^{21} cm^{-3} s^{-1}. This behavior is described quantitatively by the following relation:

$$G(\lambda, x) = a(\lambda, x) N_{phot}(\lambda, x) \tag{15}$$

Here, $G(\lambda, x)$ represents the generation rate of electron–hole pairs at a given wavelength λ and depth x within the absorber. The term $\alpha(\lambda, x)$ is the absorption coefficient, which reflects how strongly the material absorbs light at different wavelengths and depths, while $N_{phot}(\lambda, x)$ denotes the photon flux—the number of incident photons available for absorption at that wavelength and position. This equation shows that carrier generation is directly influenced by both the material's optical absorption properties and the incident light intensity. In this context, although Rb$_2$AuScBr$_6$ shows a slightly higher peak generation rate, the favorable absorption behavior of Rb$_2$AuScCl$_6$ enables it to harness a wider portion of the solar spectrum effectively, resulting in substantial exciton generation and contributing to
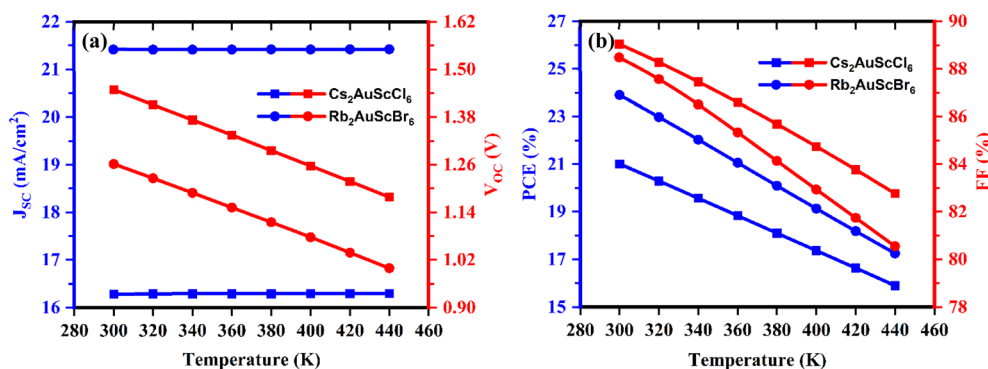

Fig. 15 Effect of temperature on performance parameters (a) V_{oc} and J_{sc}, (b) PCE and FF of (ITO/IGZO/Rb$_2$AuScBr$_6$/CBTS/Ni) and (ITO/WS$_2$/Rb$_2$AuScCl$_6$/CBTS/Ni) devices.
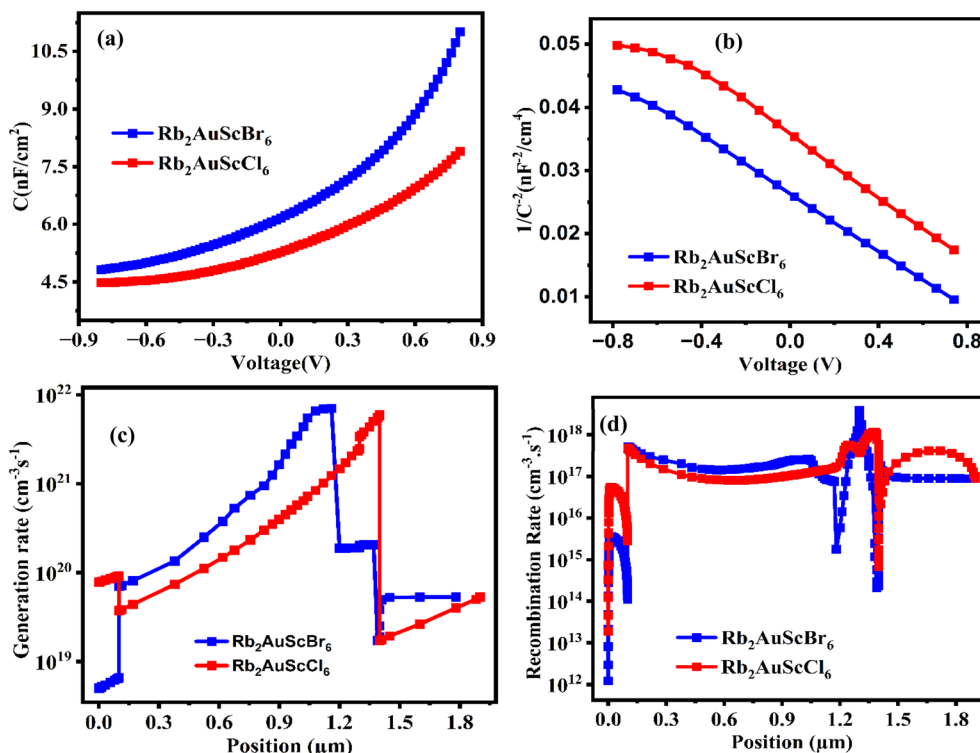
Fig. 16 (a) Capacitance, (b) Mott–Scotty plot ($1/C^2$), (c) generation, and (d) recombination of (ITO/IGZO/Rb$_2$AuScBr$_6$/CBTS/Ni) and (ITO/WS$_2$/Rb$_2$AuScCl$_6$/CBTS/Ni) devices.

an elevated J_{sc}. Fig. 16(d) shows that the Rb$_2$AuScCl$_6$-based device exhibits significantly lower recombination rates throughout both the absorber layer and the interfaces, compared to the Rb$_2$AuScBr$_6$-based device. This lower recombination indicates that fewer charge carriers are lost before contributing to current, suggesting longer carrier lifetimes and less defect-induced trapping within the material. These advantages are likely due to better crystal quality, optimized interface alignment, and reduced trap densities in Rb$_2$AuScCl$_6$. As a result, although both devices are capable of generating charge carriers efficiently under illumination, the reduced recombination in Rb$_2$AuScCl$_6$ allows more carriers to reach the electrodes and contribute to the output power. Combined with its strong dielectric properties and higher concentration of mobile carriers, these factors lead to a noticeable improvement in key photovoltaic parameters such as the V_{oc}, FF, and overall PCE. Therefore, the Rb$_2$AuScCl$_6$-based perovskite solar cell demonstrates greater promise for high-performance and stable lead-free solar technologies.[73]

3.14. Current density vs. voltage (J–V) and quantum efficiency (QE) curve

Fig. 17(a) and (b) shows the J–V characteristics of Rb$_2$AuScBr$_6$ and Rb$_2$AuScCl$_6$ based Absorber investigated perovskite solar cell structures are presented with voltage varying from 0 to 1.50 V; from which the Rb$_2$AuScBr$_6$-based PSC initially shows a current density of nearly 21.41 mA cm^{-2} and finally shows a current density of nearly 21.20 mA cm^{-2} the Rb$_2$AuScCl$_6$-based

device presents initial J_{sc} of ~16.26 mA cm^{-2} and final J_{sc} of 16.13 mA cm^{-2}. Within this analysis, we observe that compared to the initial value slightly decrease final value of J_{sc}. The initial V_{oc} is 1.28 V for Rb$_2$AuScBr$_6$ and 1.46 V for Rb$_2$AuScCl$_6$, and final V_{oc} 1.44 for Rb$_2$AuScBr$_6$ and 1.56 for Rb$_2$AuScCl$_6$ as shown in Fig. 17(a) and (b).

The red curve exhibits an improved and delayed current drop, indicating enhanced charge separation and reduced carrier recombination. Although the maximum current density is slightly lower than the initial case, the extended voltage range suggests an overall improvement in device efficiency. The final curve exhibits an improved and delayed current drop, indicating enhanced charge separation and reduced carrier recombination. Although the maximum current density is slightly lower than the initial case, the extended voltage range suggests an overall improvement in device efficiency.[74] Their maximum QE initial value is 99.91% and final value 99.81% measured at 360 nm for Rb$_2$AuScBr$_6$ and QE initial value 99.99% and final value 99.84% at 410 nm for Rb$_2$AuScCl$_6$ across both curves. In the visible spectrum (especially in the range of 360–450 nm), optimal QE of 100% is achieved for both materials. It is important to highlight that (as shown in Fig. 17(c) and (d)), QE reaches near 100% for both initial and final curves in most of the visible spectrum region, although after the wavelength of 700 nm for (Rb$_2$AuScBr$_6$) and 650 nm for (Rb$_2$AuScCl$_6$), QE drops dramatically.

However, there is a decrease in the QE for both solar cells at longer wavelengths due to recombination, which occurs when
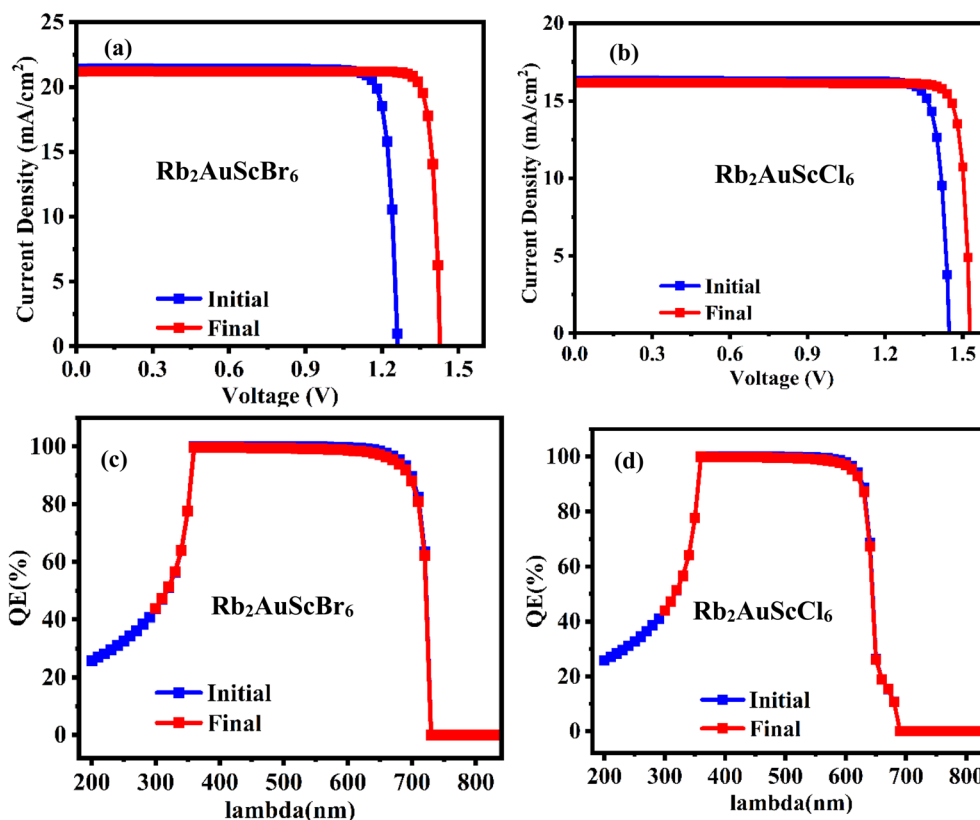
Fig. 17 (a and b) J–V characteristics and (c and d) QE curve of $Rb_2AuScBr_6$ and $Rb_2AuScCl_6$-baesd absorber initial and final devices.

charge carriers do not pass into an external circuit. The same processes that influence the collection probability also affect QE. For example, changes to the front surface can affect the carriers that are produced near the surface. High doping on the front surface layers can lead to free carrier absorption, which also has an increase in absorption, leading to a decrease in the QE in longer wavelengths.[75]

3.15. Final devices after optimization

Initially, the devices were configured as ($ITO/IGZO/Rb_2AuScBr_6/CBTS/Ni$) and ($ITO/WS_2/Rb_2AuScCl_6/CBTS/Ni$). For the Br-based absorber, IGZO exhibited superior electron transport performance with a PCE of 23.90%. Upon optimizing absorber layer parameters—including acceptor density, electron affinity, defect density, series resistance, shunt resistance, and temperature—the highest PCE of 25.81% was achieved at an acceptor density of 10^{18} cm^{-3} using IGZO as the ETL.

Further improvement was observed by replacing IGZO with alternative ETLs, when the acceptor density was maintained at 10^{18} cm^{-3}, TiO_2, ZnO, and WS_2 offered enhanced PCEs of 27.49%, 27.37%, and 27.30%, respectively. Among them, TiO_2 demonstrated the best performance, leading to the final optimized device structure for the Br-based absorber:

Glass/ITO (0.500 μm)/TiO_2 (0.030 μm)/$Rb_2AuScBr_6$ (1.200 μm)/CBTS (0.100 μm)/Ni (5.5 eV), with a PCE of 27.49% at a defect density of 10^{15} cm^{-3}.

On the other hand (Fig. 18), the Cl-based absorber initially showed the best performance with WS_2 as the ETL, yielding a PCE of 20.98%. After acceptor density optimization (10^{17} cm^{-3}), the PCE improved to 22.41% at a defect density of 10^{15} cm^{-3}. This confirmed the final optimized device configuration as: Glass/ITO (0.500 μm)/WS_2 (0.030 μm)/$Rb_2AuScCl_6$ (1.200 μm)/CBTS (0.100 μm)/Ni (5.5 eV).

3.16. Comparison with other works

In comparison with previously reported theoretical studies on lead-free perovskite solar cells, the present work demonstrates outstanding photovoltaic (PV) performance, particularly in devices based on the $Rb_2AuScBr_6$ and $Rb_2AuScCl_6$ perovskite absorbers. The optimized structure $ITO/TiO_2/Rb_2AuScBr_6/CBTS/Ni$ achieves a maximum PCE of 27.49%, with a V_{oc} of 1.428 V, (J_{sc}) of 21.280 mA cm^{-2}, and FF of 89.951%. Similarly, structures incorporating ZnO and WS_2 as ETLs, $ITO/ZnO/Rb_2AuScBr_6/CBTS/Ni$ and $ITO/WS_2/Rb_2AuScBr_6/CBTS/Ni$—achieved high PCEs of 27.37% and 27.30%, respectively. These performances significantly surpass those of other reported lead-free configurations. For instance, devices such as $ITO/PCBM/KgeCl_3/CBTS/Ni$[76] and $FTO/C_{60}/KgeCl_3/PEDOT:PSS/Ni$[77] exhibited lower efficiencies of 21.79% and 20.46%, respectively. Furthermore, structures like $FTO/ZnO/KsnI_3/CuI/Au$[78] PCE of (20.99%), $ITO/IGZO/CsSnCl_3/CBTS/Au$ PCE of (21.07%), and $ITO/WS_2/CsSnCl_3/CBTS/Au$[79] PCE of (21.32%) also reported considerably lower PCE values. Even the $FTO/PCBM/CsSnCl_2/$
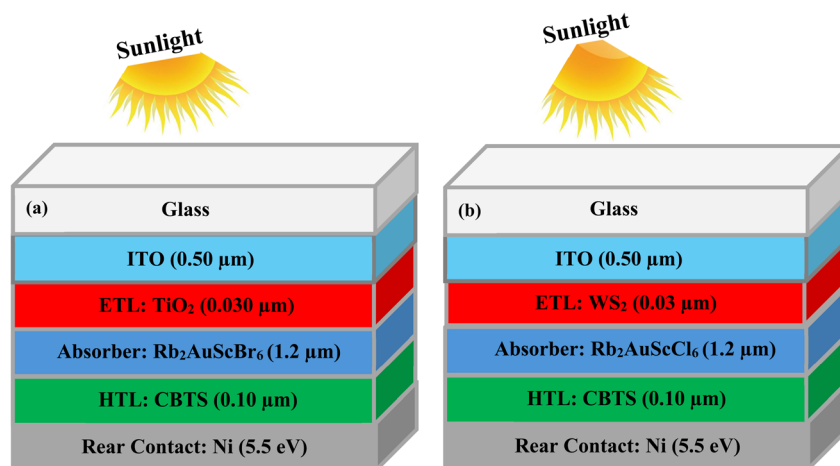
Fig. 18 The final device configuration of the absorber (a) $Rb_2AuScBr_6$ and (b) $Rb_2AuScCl_6$-based PSC.

Table 4 The comparison of PV parameters of $Rb_2AuScBr_6$- and $R_2AuScCl_6$-based solar cells

Optimized devices	Types	V_{oc} (V)	J_{sc} (mA cm^{-2})	FF (%)	PCE (%)	Ref.
ITO/TiO$_2$/Rb$_2$AuScBr$_6$/CBTS/Ni	Theo	1.428	21.280	89.951	27.49	This work
ITO/ZnO/Rb$_2$AuScBr$_6$/CBTS/Ni	Theo	1.428	21.209	90.342	27.37	This work
ITO/WS$_2$/Rb$_2$AuScBr$_6$/CBTS/Ni	Theo	1.426	21.280	89.951	27.30	This work
ITO/WS$_2$/Rb$_2$AuScCl$_6$/CBTS/Ni	Theo	1.210	22.517	83.055	22.41	This work
ITO/PCBM/KgeCl$_3$/CBTS/Ni	Theo	0.6745	41.405	78.02	21.79	72
FTO/C$_{60}$/KgeCl$_3$/PEDOT : PSS/Ni	Theo	0.632	41.13	78.71	20.46	73
FTO/ZnO/KSnI$_3$/CuI/Au	Theo	1.44	17.06	85.24	20.99	74
ITO/IGZO/CsSnCl$_3$/CBTS/Au	Theo	1.02	26.14	78.69	21.07	30
ITO/WS$_2$/CsSnCl$_3$/CBTS/Au	Theo	1.01	25.92	81.33	21.32	30
FTO/PCBM/CsSnCl$_3$/PTAA/Au	Theo	1.30	15.34	89.90	17.93	75

PTAA/Au[80] configuration yielded a much lower efficiency of 17.93%. Notably, the $Rb_2AuScCl_6$-based device.

ITO/WS$_2$/Rb$_2$AuScCl$_6$/CBTS/Ni only achieved a PCE of 22.41%, which is substantially lower than that of the Rb$_2$AuScBr$_6$-based devices. These results clearly indicate that the combination of IGZO, TiO$_2$, or ZnO as ETLs, CBTS as the HTL, and Rb$_2$AuScBr$_6$ as the absorber forms a highly promising structure for next-generation, high-efficiency, lead-free perovskite solar cells (Table 4).

4. Conclusion

This study systematically optimized lead-free PSCs employing $Rb_2AuScBr_6$ and $Rb_2AuScCl_6$ absorbers. Initial screening identified ITO/IGZO/Rb$_2$AuScBr$_6$/CBTS/Ni and ITO/WS$_2$/Rb$_2$AuScCl$_6$/CBTS/Ni as the best-performing baseline architectures. Device performance was then enhanced through absorber thickness optimization, back-contact work function tuning, doping concentration adjustment, and defect density control.

For Rb$_2$AuScBr$_6$-based PSCs, an optimal absorber thickness of ~1200 nm balanced light absorption with charge transport, achieving a peak PCE of 25.81% at an acceptor density of 10^{18} cm^{-3} and a defect density of 10^{15} cm^{-3}. Increasing the back-contact work function to 5.5 eV further improved efficiency. Substituting the IGZO ETL with TiO$_2$, ZnO, or WS$_2$ under these

optimized conditions yielded maximum PCEs of 27.49%, 27.37%, and 27.30%, respectively, with TiO$_2$ performing best.

For Rb$_2$AuScCl$_6$-based PSCs, WS$_2$ consistently provided superior performance across all optimization stages. The highest recorded efficiency was 22.41% at an acceptor density of 10^{17} cm^{-3} and defect density of 10^{15} cm^{-3}. Both material systems demonstrated minimal performance degradation under variations in series resistance, shunt resistance, and operating temperature, confirming strong electrical and thermal stability.

The comparative analysis reveals that Rb$_2$AuScBr$_6$ offers higher ultimate efficiency potential, while Rb$_2$AuScCl$_6$ provides competitive performance with robust ETL compatibility. The environmentally friendly composition of both absorbers, combined with high efficiency and operational stability, underscores their suitability as sustainable alternatives to toxic lead-based perovskites.

Given their promising efficiency, thermal stability, and non-toxic composition, these devices are particularly well-suited for building-integrated photovoltaics (BIPV), where safety, stability, and aesthetic flexibility are crucial, as well as for next-generation lightweight solar modules for portable and off-grid applications. The findings emphasize that careful device engineering, especially ETL selection, doping control, and absorber layer optimization, can enable lead-free PSCs to achieve

performance levels competitive with their lead-based counterparts, paving the way for their integration into large-scale, eco-friendly solar energy systems.

Author contributions

Md. Al-Amin: writing – original draft, data calculations, methodology, validation. A. Haque: writing – review & editing, investigation, validation. S. Mahmud: writing – review & editing, methodology, conceptualization, formal analysis, validation. M. M. Hossain: writing – review & editing, validation. M. M. Uddin: writing – review & editing, validation. M. A. Ali: writing – review & editing, supervision, project administration, validation.

Conflicts of interest

The authors declare that they have no known competing financial interests or personal relationships that could have appeared to influence the work reported in this paper.

Data availability

The datasets generated and/or analyzed during the current study are available within the article, and the raw data are available from the corresponding author upon reasonable request.

References

1 J. S. Riti and Y. Shu, Renewable energy, energy efficiency, and eco-friendly environment (R-E5) in Nigeria, *Energy Sustain. Soc.*, 2016, **6**(1), 13.

2 S. Rabhi and *et al.*, Rethinking Solar Energy: Innovations in Eco-friendly Materials, in *Breaking Boundaries: Pioneering Sustainable Solutions through Materials and Technology*, Singapore, Springer Nature Singapore, 2025, pp. 3–15.

3 A. O. Maka and J. M. Alabid, Solar energy technology and its roles in sustainable development, *Clean Energy*, 2022, **6**(3), 476–483.

4 I.-A. Vlad and A. Drăgulinescu, High Efficiency Perovskite Solar Cells Optimization, in *2023 IEEE 29th International Symposium for Design and Technology in Electronic Packaging (SIITME)*, IEEE, 2025, pp. 102–105.

5 M. K. Hossain, *et al.*, Design and Simulation of Cs_2BiAgI_6 Double Perovskite Solar Cells with Different Electron Transport Layers for Efficiency Enhancement, *Energy Fuels*, 2023, **37**(5), 3957–3979.

6 F. Ji, G. Boschloo, F. Wang and F. Gao, Challenges and Progress in Lead-Free Halide Double Perovskite Solar Cells, *Sol. RRL*, 2023, **7**(6), 2201112.

7 M. H. Miah, *et al.*, Lead-free alternatives and toxicity mitigation strategies for sustainable perovskite solar cells: a critical review, *Mater. Adv.*, 2025, **6**, 2718–2752.

8 R. Ahmad, *et al.*, Colloidal lead-free $Cs_2AgBiBr_6$ double perovskite nanocrystals: Synthesis, uniform thin-film

fabrication, and application in solution-processed solar cells, *Nano Res.*, 2021, **14**(4), 1126–1134.

9 M. I. Khan, *et al.*, Bandgap reduction and efficiency enhancement in $Cs_2AgBiBr_6$ double perovskite solar cells through gallium substitution, *RSC Adv.*, 2024, **14**(8), 5440–5448.

10 G. Volonakis, *et al.*, Lead-Free Halide Double Perovskites *via* Heterovalent Substitution of Noble Metals, *J. Phys. Chem. Lett.*, 2016, **7**(7), 1254–1259.

11 M. A. Rayhan, M. M. Hossain, M. M. Uddin, S. H. Naqib, and M. A. Ali, *DFT Exploration of Novel Direct Band Gap Semiconducting Halide Double Perovskites, $A_2AgIrCl_6$ (A = Cs, Rb, K), for Solar Cells Application*, 2024.

12 J. F. R. V. Silveira and J. L. F. Da Silva, Mixed Halide Lead-free Double Perovskite Alloys for Band Gap Engineering, *ACS Appl. Energy Mater.*, 2020, **3**(8), 7364–7371.

13 M. T. Iqbal, *et al.*, Next-Generation Materials Discovery Using DFT: Functional Innovation, *Sol. Energy Catal. Eco Toxic. Model. Sch J Eng Tech*, 2025, **7**, 454–486.

14 S. A. U. Wasti and *et al.*, *Optimization and Performance Evaluation of $Cs_2CuBiCl_6$ Double Perovskite Solar Cell for Lead-Free Photovoltaic Applications*, 2025.

15 H. Chen, *et al.*, Lead Sequestration in Perovskite Photovoltaic Device Encapsulated with Water-Proof and Adhesive Poly (ionic liquid), *ACS Appl. Mater. Interfaces*, 2023, **15**(10), 13637–13643.

16 M. K. S. Bin Rafiq, *et al.*, WS_2: a new window layer material for solar cell application, *Sci. Rep.*, 2020, **10**(1), 771.

17 M. E. Islam, M. R. Islam, S. Ahmmed, M. K. Hossain and M. F. Rahman, Highly efficient SnS-based inverted planar heterojunction solar cell with ZnO ETL, *Phys. Scr.*, 2023, **98**(6), 065501.

18 P. Patil, D. S. Mann, U. T. Nakate, Y.-B. Hahn, S.-N. Kwon and S.-I. Na, Hybrid interfacial ETL engineering using PCBM-SnS_2 for High-Performance pin structured planar perovskite solar cells, *Chem. Eng. J.*, 2020, **397**, 125504.

19 X. Zhang, *et al.*, Amorphous TiO_2 film with fiber-like structure: An ideal candidate for ETL of perovskite solar cells, *Mater. Lett.*, 2022, **324**, 132684.

20 J. Li, S. Kundu, L. Souriau, P. Bezard, R. Izmailov and F. Lazzarino, Plasma Etch of IGZO Thin Film and IGZO/SiO_2 Interface Diffusion in Inductively Coupled CH_4/Ar Plasmas, *Plasma Process. Polym.*, 2025, **22**(2), 2400186.

21 A. Mohandes and M. Moradi, Improved performance of inorganic $CsPbI_3$ perovskite solar cells with WO_3/C_{60} UTL bilayer as an ETL structure: A computational study, *Phys. Scr.*, 2024, **99**(5), 055951.

22 G. Pindolia, S. M. Shinde and P. K. Jha, Optimization of an inorganic lead free $RbGeI_3$ based perovskite solar cell by SCAPS-1D simulation, *Sol. Energy*, 2022, **236**, 802–821.

23 I. Montoya De Los Santos, *et al.*, The study of inorganic absorber layers in perovskite solar cells: the influence of CdTe and CIGS incorporation, *Sci. Rep.*, 2025, **15**(1), 10353.

24 A. Ghosh, *et al.*, Solar power conversion: CuI hole transport layer and Ba_3NCl_3 absorber enable advanced solar cell technology boosting efficiency over 30%, *RSC Adv.*, 2024, **14**(33), 24066–24081.

25 Q. Zhao, et al., Achieving efficient inverted planar perovskite solar cells with nondoped PTAA as a hole transport layer, Org. Electron., 2019, 71, 106–112.

26 C. D. Ramabadran and K. S. Sudheer, A Study on the influence of different HTL and ETL layers on the performance of a P3HT, C_{60} bulk heterojunction organic solar cell, Indian J. Phys., 2025, 99(1), 273–282.

27 C.-C. Shih and C.-G. Wu, Synergistic Engineering of the Conductivity and Surface Properties of PEDOT: PSS-Based HTLs for Inverted Tin Perovskite Solar Cells to Achieve Efficiency over 10%, ACS Appl. Mater. Interfaces, 2022, 14(14), 16125–16135.

28 M. Al-Hattab, L. Moudou, M. Khenfouch, O. Bajjou, Y. Chrafih and K. Rahmani, Numerical simulation of a new heterostructure CIGS/GaSe solar cell system using SCAPS-1D software, Sol. Energy, 2021, 227, 13–22.

29 M. Bošnjaković, Advances of sustainable energy materials: technology trends for silicon-based photovoltaic cells, Sustainability, 2024, 16(18), 7962.

30 S. Jouttijärvi, G. Lobaccaro, A. Kamppinen and K. Miettunen, Benefits of bifacial solar cells combined with low voltage power grids at high latitudes, Renew. Sustain. Energy Rev., 2022, 161, 112354.

31 Z. Song, C. Li, L. Chen and Y. Yan, Perovskite Solar Cells Go Bifacial—Mutual Benefits for Efficiency and Durability, Adv. Mater., 2022, 34(4), 2106805.

32 M. Vishnuwaran, K. Ramachandran and P. Roy, SCAPS simulated $FASnI_3$ and $MASnI_3$ based PSC solar cells: A comparison of device performance, IOP Conf. Ser.: Mater. Sci. Eng., 2025, 012048.

33 S. N. Ali, M. B. Zahran and A. A. Z. Diab, Comprehensive comparison between the experimental and simulated characteristics of the mono-crystalline silicon solar cell using SCAPS-1D, Int. J. Sci. Eng. Appl., 2023, 4(2), 165–172.

34 M. K. Hossain, et al., An extensive study on multiple ETL and HTL layers to design and simulate high-performance lead-free $CsSnCl_3$-based perovskite solar cells, Sci. Rep., 2023, 13(1), 2521.

35 A. T. Ngoupo, S. Ouédraogo, F. Zougmoré and J. M. B. Ndjaka, Numerical analysis of ultrathin Sb_2Se_3-based solar cells by SCAPS-1D numerical simulator device, Chin. J. Phys., 2021, 70, 1–13.

36 S. Karthick, S. Velumani and J. Bouclé, Chalcogenide $BaZrS_3$ perovskite solar cells: A numerical simulation and analysis using SCAPS-1D, Opt. Mater., 2022, 126, 112250.

37 M. G. Hudedmani, V. Soppimath and C. Jambotkar, A study of materials for solar PV technology and challenges, Eur. J. Appl. Eng. Sci. Res., 2017, 5(1), 1–13.

38 M. Dada and P. Popoola, Recent advances in solar photovoltaic materials and systems for energy storage applications: a review, Beni-Suef Univ. J. Basic Appl. Sci., 2023, 12(1), 66.

39 M. V. Dambhare, B. Butey, and S. V. Moharil, Solar photovoltaic technology: A review of different types of solar cells and its future trends, in Journal of Physics: Conference Series, IOP Publishing, 2025, p. 012053.

40 S. Mahmud, M. M. Hossain, M. M. Uddin and M. A. Ali, Prediction of X_2AuYZ_6 (X= Cs, Rb; Z= Cl, Br, I) double halide perovskites for photovoltaic and wasted heat management device applications, J. Phys. Chem. Solids, 2025, 196, 112298.

41 N. Vukmirović, Calculations of electron mobility in II–VI semiconductors, Phys. Rev. B, 2021, 104(8), 085203.

42 Y. Zhou and G. Long, Low Density of Conduction and Valence Band States Contribute to the High Open-Circuit Voltage in Perovskite Solar Cells, J. Phys. Chem. C, 2017, 121(3), 1455–1462.

43 S. S. Bagade, S. B. Barik, M. M. Malik and P. K. Patel, Impact of band alignment at interfaces in perovskite-based solar cell devices, Mater. Today Proc., 2023, DOI: 10.1016/j.matpr.2023.02.117.

44 P. Gupta, Band alignment studies of $Zn_{1-x}Ni_xO$/ZnO: as bilayer electron transport layer in perovskite solar cells, Opt. Mater., 2024, 150, 115305.

45 S. Mahmud, M. A. Ali, M. M. Hossain and M. M. Uddin, DFT aided prediction of phase stability, optoelectronic and thermoelectric properties of A_2AuScX_6 (A= Cs, Rb; X= Cl, Br, I) double perovskites for energy harvesting technology, Vacuum, 2024, 221, 112926.

46 X. Yu, et al., Numerical simulation analysis of the effect of energy band alignment and functional layer thickness on the performance for perovskite solar cells with $Cd_{1-x}Zn_xS$ electron transport layer, Mater. Res. Express, 2020, 7(10), 105906.

47 A. Kumar, D. Punetha and S. Chakrabarti, Performance optimization of phenylethylammonium-formamidinium tin iodide perovskite solar cell by contrasting various ETL and HTL materials, J. Nanoparticle Res., 2023, 25(3), 52.

48 Md. S. Reza, et al., Optimizing Charge Transport Layers to Enhance the Performance of Lead-Free $RbGeI_3$ Perovskite Solar Cells: A Comprehensive Analysis of ETL and HTL Engineering, Langmuir, 2025, 41(11), 7865–7885.

49 Md. S. Reza, et al., Optimizing Charge Transport Layers to Enhance the Performance of Lead-Free $RbGeI_3$ Perovskite Solar Cells: A Comprehensive Analysis of ETL and HTL Engineering, Langmuir, 2025, 41(11), 7865–7885.

50 S. Bichave, J. Mundupuzhakal, P. N. Gajjar and S. K. Gupta, Analysis of varying ETL/HTL material for an effective perovskite solar cell by numerical simulation, Mater. Today Proc., 2023, 2025.

51 U. C. Obi, D. M. Sanni and A. Bello, Effect of Absorber Layer Thickness on the Performance of Bismuth-Based Perovskite Solar Cells, Semiconductors, 2021, 55(12), 922–927.

52 N. A. A. Malek, et al., Enhanced Charge Transfer in Atom-Thick 2H–WS_2 Nanosheets' Electron Transport Layers of Perovskite Solar Cells, Sol. RRL, 2020, 4(10), 2000260.

53 Z. Chen and G. Chen, The effect of absorber thickness on the planar Sb_2S_3 thin film solar cell: Trade-off between light absorption and charge separation, Sol. Energy, 2020, 201, 323–329.

54 U. C. Obi, D. M. Sanni and A. Bello, Effect of Absorber Layer Thickness on the Performance of Bismuth-Based Perovskite Solar Cells, Semiconductors, 2021, 55(12), 922–927.

55 A. Bag, R. Radhakrishnan, R. Nekovei and R. Jeyakumar, Effect of absorber layer, hole transport layer thicknesses, and its doping density on the performance of perovskite solar cells by device simulation, *Sol. Energy*, 2020, **196**, 177–182.

56 R. S. Hall, D. Lamb and S. J. C. Irvine, Back contact materials used in thin film CdTe solar cells—A review, *Energy Sci. Eng.*, 2021, **9**(5), 606–632.

57 M. S. Jamal, *et al.*, Effect of defect density and energy level mismatch on the performance of perovskite solar cells by numerical simulation, *Optik*, 2019, **182**, 1204–1210.

58 J. Madan, S. Garg, K. Gupta, S. Rana, A. Manocha and R. Pandey, Numerical simulation of charge transport layer free perovskite solar cell using metal work function shifted contacts, *Optik*, 2020, **202**, 163646.

59 P. Ru, *et al.*, High Electron Affinity Enables Fast Hole Extraction for Efficient Flexible Inverted Perovskite Solar Cells, *Adv. Energy Mater.*, 2020, **10**(12), 1903487.

60 A. V. Mumyatov and P. A. Troshin, A review on fullerene derivatives with reduced electron affinity as acceptor materials for organic solar cells, *Energies*, 2023, **16**(4), 1924.

61 Q. Guo, *et al.*, Effect of Energy Alignment, Electron Mobility, and Film Morphology of Perylene Diimide Based Polymers as Electron Transport Layer on the Performance of Perovskite Solar Cells, *ACS Appl. Mater. Interfaces*, 2017, **9**(12), 10983–10991.

62 K. C. Fong, K. R. McIntosh and A. W. Blakers, Accurate series resistance measurement of solar cells, *Prog. Photovolt. Res. Appl.*, 2013, **21**(4), 490–499.

63 M. Wolf and H. Rauschenbach, Series resistance effects on solar cell measurements, *Adv. Energy Convers.*, 1963, **3**(2), 455–479.

64 K. Rajkanan and J. Shewchun, A better approach to the evaluation of the series resistance of solar cells, *Solid-State Electron.*, 1979, **22**(2), 193–197.

65 J. D. Servaites, S. Yeganeh, T. J. Marks and M. A. Ratner, Efficiency Enhancement in Organic Photovoltaic Cells: Consequences of Optimizing Series Resistance, *Adv. Funct. Mater.*, 2010, **20**(1), 97–104.

66 A. D. Dhass, E. Natarajan, and L. Ponnusamy, Influence of shunt resistance on the performance of solar photovoltaic cell, in *2012 International Conference on Emerging Trends in Electrical Engineering and Energy Management (ICETEEEM)*, IEEE, 2025, pp. 382–386.

67 M. Barbato, M. Meneghini, A. Cester, G. Mura, E. Zanoni and G. Meneghesso, Influence of shunt resistance on the performance of an illuminated string of solar cells: theory, simulation, and experimental analysis, *IEEE Trans. Device Mater. Reliab.*, 2014, **14**(4), 942–950.

68 M. Fortes, E. Comesana, J. A. Rodriguez, P. Otero and A. J. Garcia-Loureiro, Impact of series and shunt resistances in amorphous silicon thin film solar cells, *Sol. Energy*, 2014, **100**, 114–123.

69 C. M. Proctor and T.-Q. Nguyen, Effect of leakage current and shunt resistance on the light intensity dependence of organic solar cells, *Appl. Phys. Lett.*, 2015, **106**(8), 2025.

70 P. Singh and N. M. Ravindra, Temperature dependence of solar cell performance—an analysis, *Sol. Energy Mater. Sol. Cells*, 2012, **101**, 36–45.

71 Q. Meng, *et al.*, Effect of temperature on the performance of perovskite solar cells, *J. Mater. Sci. Mater. Electron.*, 2021, **32**(10), 12784–12792.

72 S. Ravishankar, Z. Liu, U. Rau and T. Kirchartz, Multilayer Capacitances: How Selective Contacts Affect Capacitance Measurements of Perovskite Solar Cells, *PRX Energy*, 2022, **1**(1), 013003.

73 J. Chen and N. Park, Causes and Solutions of Recombination in Perovskite Solar Cells, *Adv. Mater.*, 2019, **31**(47), 1803019.

74 S. Mudgal, S. Singh, and V. K. Komarala, Interfacial spectral response under voltage and light bias to analyse low voltage in amorphous-crystalline silicon heterojunction solar cell with S-shape characteristics, in *2018 IEEE 7th World Conference on Photovoltaic Energy Conversion (WCPEC)(a Joint Conference of 45th IEEE PVSC, 28th PVSEC & 34th EU PVSEC)*, IEEE, 2025, pp. 2158–2161.

75 L. Liu, *et al.*, Quantum efficiency and temperature coefficients of GaInP/GaAs dual-junction solar cell, *Sci. China, Ser. E: Technol. Sci.*, 2009, **52**(5), 1176–1180.

76 M. Tarekuzzaman, *et al.*, An in-depth investigation of lead-free KGeCl$_3$ perovskite solar cells employing optoelectronic, thermomechanical, and photovoltaic properties: DFT and SCAPS-1D frameworks, *Phys. Chem. Chem. Phys.*, 2024, **26**(43), 27704–27734.

77 M. E. Sarhani, T. Dahame, M. L. Belkhir, B. Bentria and A. Begagra, AB-INITIO study of electronic, mechanical, optical and thermoelectric properties of KGeCl$_3$ for photovoltaic application, *Heliyon*, 2023, **9**(9), e19808.

78 F. B. Sumona, *et al.*, Optimization of Perovskite-KSnI$_3$ Solar Cell by Using Different Hole and Electron Transport Layers: A Numerical SCAPS-1D Simulation, *Energy Fuels*, 2023, **37**(23), 19207–19219.

79 S. Srivastava, A. K. Singh, P. Kumar and B. Pradhan, Comparative performance analysis of lead-free perovskite solar cells by numerical simulation, *J. Appl. Phys.*, 2022, **131**(17), 175001.

80 Y. Selmani and L. Bahmad, Computational study of mixed halide perovskites CsSnX$_3$ (X= Br, Cl, mixed halides) for optoelectronic and thermoelectric applications: A DFT and Boltzmann transport methods, *Mater. Sci. Eng., B*, 2025, **319**, 118373.